Published for SISSA by Springer

Received: June 18, 2019
Accepted: October 8, 2019
Published: October 31, 2019

Light mediators in anomaly free $\mathrm{U}(1)_X$ models. Part II. Constraints on dark gauge bosons

F.C. Correia[a] **and Svjetlana Fajfer**[b,c]

[a] *Institut für Physik, Technische Universität Dortmund, D-44221 Dortmund, Germany*
[b] *Department of Physics, University of Ljubljana, Jadranska 19, 1000 Ljubljana, Slovenia*
[c] *J. Stefan Institute, Jamova 39, P.O. Box 3000, 1001 Ljubljana, Slovenia*

E-mail: fagner.correia@tu-dortmund.de, svjetlana.fajfer@ijs.si

Abstract: We consider experimental constraints in the MeV region in order to determine the parameter space for the $\mathrm{U}(1)_X$ extension of the Standard Model, presented in the first part of our work. In particular, we focus on the model UV-completed by cold WIMPs. We conclude that the electron anomalous magnetic moment and the neutrino trident production provide the most stringent bounds to $g_X^2 \sim 10^{-6}$ in the mass interval below the di-muon threshold. By allowing the axial-vector coupling of the dark gauge boson Z', the interference effect with the SM gauge bosons may reduce the bounds coming from the neutrino trident production. At the same time, such coupling allows a region of the parameter space already favored both by the relic abundance and by the discrepancy between experimental result and theoretical prediction for the muon anomalous magnetic moment. We emphasize that light-Z' interactions, non-universal for the two first lepton families, necessarily create a difference in the proton charge radius measured in the Lamb shift of the e-hydrogen and μ-hydrogen. Finally, we determine the effects of the new gauge boson on the forward-backward asymmetry in $e^+e^- \to \bar{f}f$, $f = \mu, \tau$, and on the leptonic decays $M \to j\nu_j l^+ l^-$, where $M = \pi, K, D, D_s, B$ and $j, l = e, \mu$.

Keywords: Beyond Standard Model, Higgs Physics, Neutrino Physics

ArXiv ePrint: 1905.03872

Open Access, © The Authors.
Article funded by SCOAP[3].

https://doi.org/10.1007/JHEP10(2019)279

JHEP10(2019)279

Contents

1 Introduction **1**

2 U(1)$_X$ coupling to right-handed fermions **3**

3 Low-energy constraints **5**
- 3.1 ρ parameter 5
- 3.2 Proton charge radius in the U(1)$_X$ model 6
- 3.3 $M^+ \to \mu^+$ invisibles 8
- 3.4 $(g-2)_e$ 10
- 3.5 $(g-2)_\mu$ 12
- 3.6 $K_{\mu\nu e^+e^-}$ 14
- 3.7 Neutrino trident production 14
- 3.8 χ relic abundance 16

4 Outlook **18**
- 4.1 Parity non-conserving observables 18
- 4.2 Leptonic meson decays: $M \to l'\nu_{l'}ll$ 22

5 Conclusion **23**

A Feynman rules **25**

B Decay width **26**

C Phase space integration for the neutrino trident production **27**

JHEP10(2019)279

1 Introduction

Phenomenology of U(1) gauge bosons X_μ (see e.g. [1–9]) is, in general, very dependent on the particle content and the X-hypercharge assignment of the fundamental theory. The canonical requirements for the formulation of an ultraviolet (UV) model, such as to be anomaly free and to recover the Standard Model (SM) fermion mass matrices, indicates the presence of new scalars and stable fermions even in minimal extensions like the Two Higgs Doublet Model (2HDM). Furthermore, in order to cancel the triangle anomalies per generation, it is common to introduce new right-handed fermions. Motivated by the existence of discrepancies related to the muonic interactions, by charging the second generation under U(1)$_X$, we have found an appropriate theoretical framework to discuss either dark photons or Z' gauge bosons. The model must contain at least two Higgs doublets and one scalar singlet [10], as a condition to recover a consistent fermion mass spectrum. Apart

from its simplicity, the $\mathrm{U}(1)_X$ SM extension is commonly found in different models as the first step of a gauge breaking scheme, like, for instance, in Grand Unified Theories E_6, where $E_6 \to \mathrm{SO}(10) \otimes \mathrm{U}(1) \to \mathrm{SU}(5) \otimes \mathrm{U}(1) \otimes \mathrm{U}(1) \to SM \otimes \mathrm{U}(1)$.

Guided by our theoretical analysis of $\mathrm{SM} \otimes \mathrm{U}(1)_X$ theories, in this paper we describe the constraints from the existing experimental data on the dark gauge boson phenomenology at the low energies (MeV regime) [11]. We first consider leptonic interactions and provide the detailed expressions for the computation of the most stringent processes. In Part I of our work we present how the set of X_μ gauge bosons can be separated into A' - including dark photons - and the Z' subsets, depending whether they have axial couplings with fermions or not [12]. In the minimal dark photon phenomenology [13], only three new parameters are present, namely, the kinetic-mixing coupling, the mass of dark photon A' and its branching fraction into invisibles. In the more general case when SM fields are charged under X, the parameter space is increased by at least two parameters - the gauge coupling, and the new breaking scales. The presence of dark photon leads to small corrections of Quantum Electrodynamic (QED) quantities and is commonly favored in current experimental searches, for falsifiability reasons and safety from parity-violating effects. Notwithstanding, we aim to explicitly obtain the dependence of axial couplings on the model parameters and why their effects must be suppressed. We also check what is the effect of axial couplings in the decay width of Z' into dark matter candidates. In the chiral $\mathrm{U}(1)_X$ model, Lepton Flavor Violation (LFV) is directly suppressed through the presence of a flavor matrix $\mathbb{F}$. For instance, by X-charging the second generation of the right-handed fermions and selecting the element $\mathbb{F}_{22} = 1$, we immediately achieve that no LFV emerges at tree-level.

The analysis of section 3 is performed under the hypothesis that there is a light X_μ boson below the di-muon threshold ($\sim 10 - 200\,\mathrm{MeV}$), whose effects can be detected for couplings of the order $g_X \sim 10^{-4} - 10^{-1}$. If this hypothesis holds, the gauge boson existence must be associated to one specific point of the most favored (less excluded) parameter space, in the plane defined by m_X and g_X^2. We will see that the search for the most favored parameter planes will imply, for instance, that the fermionic dark matter candidate χ is lighter than the new vector, once the decaying channel $X \to \bar{\chi}\chi$ is open. In addition, the strong bounds from the electron anomalous magnetic moment [7] can be reduced in the vicinity of the poles, which emerge in the calculations of the $(g-2)_e$, provided by the presence of axial couplings. Under standard considerations for the relic density computation [14], this feature would severely restrict dark photon models coupled to dark matter fermionic candidates. A similar conclusion is reached from the neutrino trident production [3].

We denote by X_μ the new and generic gauge boson, while Z' and A' are assigned according to the presence or absence of axial-couplings, respectively, whenever the distinction is necessary in our analysis. In section 4.1 we calculate the forward-backward asymmetry for $\bar{e}e \to \bar{f}f$, which is relevant in the studies of light Z' physics. In section 4.2 we make predictions for leptonic meson decay widths for $M \to j\nu_j\bar{l}l$, with $M = \pi, K, D, D_s B$ and $j, l = e, \mu$, in the framework of $SM \otimes \mathrm{U}(1)_X$. Finally, section 5 contains a summary of our results.

JHEP10(2019)279

2 $\mathrm{U}(1)_X$ coupling to right-handed fermions

The present work considers a number of the most stringent constraints coming from the flavor physics in the MeV regime, applied for a particular $\mathrm{U}(1)_X$ SM extension which exclusively charges the second generation of all right-handed (RH) fermion species. Here we summarize the important vertexes, necessary for the computation presented in the next section. The fermion-gauge interactions are described by:

$$\mathcal{L}_{kin} \supset i\Big[\overline{L}_{\alpha L}\not{D}L_{\alpha L} + \overline{Q}_{\alpha L}\not{D}Q_{\alpha L} + \bar{l}_{\alpha R}\not{D}l_{\alpha R} + \bar{d}_{\alpha R}\not{D}d_{\alpha R} + \overline{u}_{\alpha R}\not{D}u_{\alpha R} + \overline{\chi}_R\not{D}\chi_R\Big], \quad (2.1)$$

where $\alpha = 1, 2, 3$, L, Q are lepton and quark isospin doublets, while l, u, d are the lepton, d-type and u-type fermion singlets, respectively. The covariant derivative D_μ is introduced as

$$D_\mu = \partial_\mu - ig(W^+\mathbb{I}_+ + W^-\mathbb{I}_-) - ie\mathbb{Q}A_\mu - ig_Z Z_\mu - ig_R X_\mu. \quad (2.2)$$

The new SU(2) singlet and stable fermion, χ_R, is required for the treatment of quantum anomalies. The couplings in the mass basis are dependent on two independent angles, i.e.

$$e\mathbb{Q} = g s_\phi \tau^3 + g_Y c_\phi Y, \quad (2.3a)$$

$$g_Z = c_\theta g_Z^{\mathrm{SM}} + s_\theta(\kappa Y + g_X X), \quad (2.3b)$$

$$g_R = s_\theta g_Z^{\mathrm{SM}} - c_\theta(\kappa Y + g_X X), \quad (2.3c)$$

where g, g_Y, g_X are the weak couplings and τ_3 is the SU(2) generator. We use $c_\phi \equiv cos\phi$ and $s_\phi \equiv sin\phi$. The quantum numbers Y and X are related to the $\mathrm{U}(1)_Y$ and $\mathrm{U}(1)_X$ parts of the $\mathrm{SM} \otimes \mathrm{U}(1)_X$ gauge group. The parameter $\kappa = g_Y\epsilon$ is the coupling resulting from the $\mathcal{L}_m = \frac{\epsilon}{2}B^Y_{\mu\nu}B^{X\mu\nu}$ kinetic mixing term, while $g_Z^{\mathrm{SM}} = \frac{g}{c_\phi}(\tau_3 - s_\phi^2\mathbb{Q})$. There are two Higgs doublets and a singlet in the model, denoted by:

$$\phi_0 = \begin{pmatrix} \varphi_0^+ \\ \frac{v_0+H_0+i\chi_0}{\sqrt{2}} \end{pmatrix}, \qquad \phi_X = \begin{pmatrix} \varphi_X^+ \\ \frac{v_X+H_X+i\chi_X}{\sqrt{2}} \end{pmatrix}, \qquad s = \frac{v_s + H_s + i\chi_s}{\sqrt{2}}. \quad (2.4)$$

with the following hypercharges

$$Y_0 = Y_X = \frac{1}{2}, \quad X_0 = 0, \quad X_X = -1, \quad Y_s = 0 \quad X_s = 1\,. \quad (2.5)$$

The vacuum expectation values v_0, v_X are the weak breaking scales assumed to be related to the SM $v^2 = v_0^2 + v_X^2$. The full reproduction of QED and the introduction of a new breaking scale, larger than the SM weak scale, allow the angles to be parametrized as:

$$s_\phi = \frac{g_Y}{\sqrt{g^2 + g_Y^2}}, \qquad s_\theta \approx \frac{|2g_X c_\beta^2 - \kappa|}{\bar{g}}\left[1 - \frac{m_X^2}{m_Z^2}\right]^{-1}. \quad (2.6)$$

and $c_\beta^2 = \frac{v_X^2}{v^2}$. The parameter s_θ regulates the NP effects in the neutral currents and it must be a small parameter. The $g_X X$ term of eq. (2.3) operates for RH fields and generates a

JHEP10(2019)279

so-called flavor matrix $\mathbb{F}$, encompassing the flavor changing (FCNC) and non-universality effects in the theory. $\mathbb{F}$ emerges after the field redefinition $f_R \to V_{fR} f'_R \equiv V_{fR} f_R$, where $f = (f_1, f_2, f_3)$:

$$\mathcal{L}_{kin} \supset -c_\theta g_X \Big[\overline{u}_R \mathbb{F}^U \gamma^\mu u_R \; + \overline{d}_R \mathbb{F}^D \gamma^\mu d_R \; + \overline{l}_R \mathbb{F}^l \gamma^\mu l_R \Big] X_\mu, \tag{2.7}$$

such that $(\mathbb{F}^f)_{ij} = X^f (V^\dagger_{fR})_{i2} (V_{fR})_{2j}$, with $\mathrm{Tr}[\mathbb{F}^f] = \mathrm{Tr}[\mathbb{X}^f] = X^f$, where X^f is the X-hypercharge of the particular fermion type. From the definition

$$|\mathbb{F}^f| \equiv X^f \begin{pmatrix} |V_{fR}|^2_{21} & |V_{fR}|_{21}|V_{fR}|_{22} & |V_{fR}|_{21}|V_{fR}|_{23} \\ |V_{fR}|_{21}|V_{fR}|_{22} & |V_{fR}|^2_{22} & |V_{fR}|_{22}|V_{fR}|_{23} \\ |V_{fR}|_{21}|V_{fR}|_{23} & |V_{fR}|_{22}|V_{fR}|_{23} & |V_{fR}|^2_{23} \end{pmatrix}, \tag{2.8}$$

one can verify that the $\mathbb{F}$ diagonal elements control the amount of Lepton Flavor Violation (LFV) predicted by the model.

In summary, the New Physics (NP) effects in flavor are dominated by X_μ interactions, which can be represented by[1]

$$\mathcal{L} \supset \frac{1}{2} \, \overline{f} \, \gamma_\mu (x^f_V + x^f_A \gamma^5) \, f \, X^\mu. \tag{2.9}$$

The couplings $x^f_{V,A}$ can be extracted by replacing in eq. (2.2) and eq. (2.1) the following hypercharge assignment:

- Y hypercharges:

$$Y_L = -\frac{1}{2}, \quad Y_Q = \frac{1}{6}, \quad Y_l = -1, \quad Y_\chi = 0, \quad Y_u = \frac{2}{3}, \quad Y_d = -\frac{1}{3}, \tag{2.10}$$

- X hypercharges (the second generation receives the charges under $\mathrm{U}(1)_X$):

$$X_L = 0, \quad X_Q = 0, \quad X_{e2} = 1, \quad X_{\chi_R} = -1, \quad X_{u2} = -1, \quad X_{d2} = 1, \tag{2.11}$$

  where the remaining RH fields uncharged.

For completeness, we present the quarks and leptons vector and axial-vector couplings

$$x^U_V = g \frac{s_\theta}{c_\phi} \left(\frac{1}{2} - \frac{4}{3} s^2_\phi \right) - c_\theta \kappa \frac{5}{6} - c_\theta g_X \mathbb{F}^U_{ii}, \tag{2.12a}$$

$$x^U_A = g \frac{s_\theta}{c_\phi} \left(-\frac{1}{2} \right) - c_\theta \kappa \frac{1}{2} - c_\theta g_X \mathbb{F}^U_{ii}, \tag{2.12b}$$

$$x^D_V = g \frac{s_\theta}{c_\phi} \left(-\frac{1}{2} + \frac{2}{3} s^2_\phi \right) + c_\theta \kappa \frac{1}{6} - c_\theta g_X \mathbb{F}^D_{ii}, \tag{2.12c}$$

$$x^D_A = g \frac{s_\theta}{c_\phi} \left(\frac{1}{2} \right) + c_\theta \kappa \frac{1}{2} - c_\theta g_X \mathbb{F}^D_{ii}, \tag{2.12d}$$

$$x^l_V = g \frac{s_\theta}{c_\phi} \left(-\frac{1}{2} + 2 s^2_\phi \right) + c_\theta \kappa \frac{3}{2} - c_\theta g_X \mathbb{F}^l_{ii}, \tag{2.12e}$$

[1] NP in Z interactions are doubled suppressed by $s_\theta g_X \approx g^2_X$.

JHEP10(2019)279

$$x_A^l = g\frac{s_\theta}{c_\phi}\left(\frac{1}{2}\right) + c_\theta\kappa\frac{1}{2} - c_\theta g_X \mathbb{F}^l_{ii}, \tag{2.12f}$$

$$x_V^\nu = -x_A^\nu = g\frac{s_\theta}{c_\phi}\left(\frac{1}{2}\right) + c_\theta\kappa, \tag{2.12g}$$

$$x_V^\chi = x_A^\chi = c_\theta g_X. \tag{2.12h}$$

We emphasize that the effects of additional new scalar fields are considered to be negligible, in contrast with those coming from the χ fermion coupling to X_μ.

X_μ interactions with charged hadrons The interaction of a new dark gauge boson X_μ with charged hadrons can be obtained by using the gauge principle of the QED Lagrangian, and by rotating the Abelian gauge field like

$$B_\mu^Y \to B_\mu^Y + \epsilon B_\mu^X, \tag{2.13}$$

which brings the kinetic mixing, at first order in ϵ, into a diagonal form. In other words, after the above transformation, the QED covariant derivative $D_\mu = \partial_\mu - ieqA_\mu$ is extended to

$$D_\mu \overset{(2.13)}{\to} \partial_\mu - ieqA_\mu + iqc_\phi^2\kappa X_\mu, \tag{2.14}$$

where $\kappa = g_Y\epsilon$. We neglect second order terms in the small parameters. The shift will allow us to compute the inner X-bremsstrahlung from a charged hadron. We present in section 4.2 its importance in the case of the $M \to \mu\nu ee$ meson decays, for $M = \pi, K, D, D_s$ and B.

3 Low-energy constraints

3.1 ρ parameter

The dependence of the W-boson mass on the coupling and vacuum expectation values (v.e.v) reproduces the Standard Model value at tree-level, i.e.

$$m_W^2 = \frac{g^2v^2}{4}, \quad \text{with } v^2 \equiv v_X^2 + v_0^2. \tag{3.1}$$

In the limit of vanishing new couplings, the Z-boson mass is SM-like, while the mass of X_μ gauge boson becomes $M_X^2 \to g_X^2\bar{v}^2 + \kappa^2v^2/4$ (with $\bar{v}^2 \equiv v_X^2 + v_s^2$, defined in eq. (2.21) of the Part I). The ρ parameter is defined by three observables, namely m_W, m_Z and the weak mixing angle, through the expression $\rho = \frac{m_W^2}{m_Z^2c_w^2}$. We use notation $cos\theta_w \equiv c_w$. In the SM these parameters are connected, such that at tree-level $\rho = 1$. Within $\mathrm{SM}\otimes\mathrm{U}(1)_X$ theories, if the couplings g and g_Y are assumed to take the SM values, or equivalently $c_\phi \equiv c_w$, the Z mass parameter approaches $(m_Z^2)_{\mathrm{SM}}$ from the right, i.e. $(m_Z^2)_X > (m_Z^2)_{\mathrm{SM}}$, which leads to a suppression in ρ. In order to find how the ρ parameter differs from unity, we can write m_Z as

$$m_Z^2 \approx \frac{v^2}{4}\bar{g}^2\left(1 + \frac{a_2^2}{\bar{g}^2 - a_1}\right) \to \frac{v^2}{4}\bar{g}^2\left(1 + s_\theta^2\right), \tag{3.2}$$

JHEP10(2019)279

with $a_1 \equiv 4\left[g_X^2 \frac{\bar{v}^2}{v^2} - g_X \kappa c_\beta^2\right] + \kappa^2$, $a_2 \equiv 2 g_X c_\beta^2 - \kappa$. The last step recalls eq. (2.6) and the light mass condition $a_1 \ll \bar{g}^2$. By relying on the above result and using the eq. (3.1) in the definition of ρ , it follows that

$$\rho_X^{\text{tree}} \approx c_\theta^2, \tag{3.3}$$

which cannot reach the central value of the experimental measurement [15] $\rho \in 1.00040(24)$. Nevertheless, at two sigma level one can demand $0.99992 < c_\theta^2 \leq 1$, i.e.

$$s_\theta^2 < 8 \times 10^{-5}. \tag{3.4}$$

Hence, it follows the genuine smallness of the θ angle at tree-level.

3.2 Proton charge radius in the $\mathrm{U}(1)_X$ model

The proton radius can be extracted from the comparison of the theoretical prediction and the measured value for the Lamb shift in muoninc and atomic hydrogen. The result can be expressed as a sum of independent physical contributions, i.e.

$$\Delta E|_{th}^l = \delta E_a^l + \delta E_b^l + \cdots + \lambda^l \langle r_p^2 \rangle|_l, \tag{3.5}$$

where $l = \mu, e$ accounts for the two types of hydrogen and the last term corresponds the correction due to the finite-size of charge distribution in the proton. At leading order λ^l is given by

$$\lambda^l = \frac{2\alpha}{3 a_l^3 n^3} \left(\delta_{P0} - \delta_{S0}\right), \tag{3.6}$$

where $n = 2$ for $2P - 2S$ and $a_l = (\alpha m_{lp})^{-1}$ is the Bohr radius of the system with reduced mass $m_{lp} = \frac{m_l m_p}{m_l + m_p}$. Numerically $\lambda^\mu = -5.2012 \ \ \text{MeV}\,\text{fm}^{-2}$. The proton charge radius is derived from the condition

$$\Delta E|_{th}^l = \Delta E|_{exp}^l, \tag{3.7}$$

with the r.h.s. denoting the experimental value of the Lamb shift in the l-hydrogen. For instance, in the muonic hydrogen [16]

$$\Delta E|_{exp}^\mu = 202.3706(23) \text{ MeV}. \tag{3.8}$$

On the theoretical side, the proton charge distribution is considered to affect the effective potential defining the μ-hydrogen states, whose Lamb shift is estimated to be (see [16])

$$\Delta E|_{th}^\mu = 206.0336(15) + 0.0332(20) - 5.2275 \langle r_p^2 \rangle. \tag{3.9}$$

Here the first term summarizes the vacuum polarization contributions and recoil effects, while the second includes a two-photon exchange contribution. The proton puzzle denotes the difference in the solutions of eq. (3.7) for both eH and μH systems, which provides[2]

$$\sqrt{\langle r_p^2 \rangle}|_\mu = 0.84087(39) \text{ fm} \qquad [16] \tag{3.10a}$$

$$\sqrt{\langle r_p^2 \rangle}|_e = 0.8758(77) \text{ fm} \qquad \text{CODATA-2010 [18]} \tag{3.10b}$$

[2] After the publication of this work, a new measurement of the atomic hydrogen Lamb shift was announced by [17].

JHEP10(2019)279

Note that the level of precision in the μH is one order of magnitude higher than in eH. The above results are obtained when no New Physics effects are included. In the present work we accommodate this discrepancy through the NP contribution in eq. (3.7), whose l.h.s. may be rewritten as

$$\Delta E|^l_{th} = \delta E^l_0 + \delta E^l_X + \lambda^l \langle r_p^2 \rangle|^X_l \tag{3.11}$$

where δE^l_0 sums up the errors of the results in eq. (3.10), and now

$$\langle r_p^2 \rangle|^X_\mu = \langle r_p^2 \rangle|^X_e . \tag{3.12}$$

Moreover, from eq. (3.11) the difference between the "X" and QED frameworks can be expressed as a small deviation δ^X_l:

$$\langle r_p^2 \rangle|^X_l = \langle r_p^2 \rangle|_l - \delta^X_l , \tag{3.13}$$

with

$$\delta^X_l \equiv \frac{\delta E^l_X}{\lambda^l} . \tag{3.14}$$

In summary, a constraint on the proton radius is imposed by eq. (3.12), i.e.

$$\delta^X_e - \delta^X_\mu = \langle r_p^2 \rangle|_e - \langle r_p^2 \rangle|_\mu . \tag{3.15}$$

In general, the correction δ^X_l is derived as the deviation from the Coulomb potential due to the exchange of a massive vector boson X_μ, or ([19])

$$V^l_X(r) = \frac{g_l g_p}{e^2} \frac{\alpha e^{-m_X r}}{r} , \tag{3.16}$$

with a correspondent shift in $2P - 2S$ given by [20]

$$\delta E^l_X = \int dr \; V^l_X(r) \left(|R_{21}(r)|^2 - |R_{20}(r)|^2 \right) r^2 = -\frac{\alpha}{2a_l^3} \left(\frac{g_l g_p}{e^2} \right) \frac{f(a_l m_X)}{m_X^2} . \tag{3.17}$$

Above, $|R_{2i}|^2$ are the radial wave-functions corresponding to the states P and S, while g_l, g_p are the lepton and proton couplings with X_μ, respectively and $f(x) = \frac{x^4}{(1+x)^4}$ [19]. The parameter $a_l = (\alpha m_{lp})^{-1}$ denotes the Bohr radius, with m_{lp} denoting the reduced mass of the $l - p$ system, and implies $a_\mu \sim 1.44$, i.e. $\sim \frac{m_\mu}{m_e}$ smaller than a_e. Therefore, for $m_X > 10\,\text{MeV}$ one can approximate $f(x) \sim 1$. From eq. (3.14) it follows that

$$\delta^X_l = 6 \left(\frac{g_l g_p}{e^2} \right) \frac{f(a_l m_X)}{m_X^2} \tag{3.18}$$

and a *proton curve* is defined by

$$6 \frac{g_p}{e^2} \frac{(g_e - g_\mu)}{m_X^2} = \langle r_p^2 \rangle|_e - \langle r_p^2 \rangle|_\mu , \tag{3.19}$$

which, in principle, can be solved by an attractive force (i.e. $\text{sgn} g_p = -\text{sgn} g_l$) strongly coupled with muons. In the $\text{SM} \otimes \text{U}(1)_X$ framework, and in the limit $f(x) \sim 1$, the sgn g_p

JHEP10(2019)279

must be opposite only to the non-universal part of the X^μ coupling. The couplings g_p and g_l, extracted from eq. (2.14) and eq. (2.12e) respectively, are given by:

$$g_p = -c_\phi^2 \kappa, \qquad g_l = \frac{x_V^l}{2}. \tag{3.20}$$

For simplicity $\mathbb{F}_{\tau\tau}$ may be set to 0, such that $\mathbb{F}_{\mu\mu} + \mathbb{F}_{ee} = 1$, what reduces the proton curve to

$$6\frac{g_p g_X}{e^2}\frac{2\mathbb{F}_{\mu\mu} - 1}{m_X^2} = 0.060(13)\ \text{fm}^2. \tag{3.21}$$

In figure 3 we present two examples for the 2σ favored region allowed by the current experimental results for the proton radius,[3] with the fixed parameters $(c_\beta, \kappa, \mathbb{F}_{\mu\mu}) = (0.8, -4g_X, 1)$ and $(c_\beta, \kappa, \mathbb{F}_{\mu\mu}) = (0.8, -g_X, 1)$. We emphasize that, even in the absence of the experimental discrepancy in eq. (3.10), any theory of lepton non-universality in the first two generations will imply, from eq. (3.11), a non-zero contribution to the Lamb shift in the l-hydrogen system and, therefore, it will impose strong constraints on these couplings in the MeV range.

3.3 $M^+ \to \mu^+$ invisibles

In this section we compare the experimentally measured decay width for $K \to \mu Y$ (Y denotes invisible states), and the theoretical prediction for the decay width of $K \to \mu^+ \nu_\mu \chi\bar{\chi}$. The narrow-width approximation (NWA) is assumed to be valid in the region where $m_X > 2m_\chi$, i.e when e^+e^-, $\nu\bar{\nu}$ and $\chi\bar{\chi}$ are the only directly accessible decay products of X_μ. Hence the differential decay width may be determined using

$$d\Gamma(K \to \mu\nu\chi\bar{\chi}) = \frac{1}{3} d\Gamma(K \to \mu\nu X)\text{BR}(X \to \chi\bar{\chi}). \tag{3.22}$$

The dominant contributions to the decay amplitude are presented in figure 1(a,b). The Feynman's rules for the vertexes related to figure 1(a,b) are given in appendix A and they lead to the amplitudes

$$\mathcal{M}_a = \left(\frac{G_F}{2\sqrt{2}} f_M V_{\text{UD}}^*\right) \frac{\epsilon_X^{\mu *}}{q_{23}^2 - m_l^2} \Big\{ (x_V^l + x_A^l) m_l \left[\bar{u}_\nu (1+\gamma_5)\left((\not{p}_2 + m_l)\gamma_\mu + 2p_{3\mu}\right) v_l\right] - (x_V^l - x_A^l) q_{23}^2 \left[\bar{u}_\nu (1+\gamma_5)\gamma_\mu v_l\right] \Big\} \tag{3.23a}$$

$$\mathcal{M}_b = \left(\frac{G_F}{\sqrt{2}} f_M V_{\text{UD}}^*\right) (c_\phi^2 \kappa) \left[(k+q)\cdot \epsilon_X^*\right] \frac{m_l}{q^2 - M^2} \left[\bar{u}_\nu (1+\gamma_5) v_l\right], \tag{3.23b}$$

where $q = p_1 + p_3$ and $q_{23} = p_2 + p_3$, f_M are meson decay constants and V_{UD} stands for the CKM matrix element present in the particular decay mode. As a cross-check one can prove that the gauge invariance holds by replacing the dark gauge boson X_μ by the photon field through $x_V^l \to 2e, x_A^l \to 0$ and $c_\phi^2 \kappa \to e$, such that $\epsilon_\mu(\mathcal{M}_a^\mu + \mathcal{M}_b^\mu) \to p_{2\mu}(\mathcal{M}_a^\mu + \mathcal{M}_b^\mu) = 0$.

[3] Note that since $g_p = -c_\phi^2 \kappa$, a force strongly coupled to electrons could also explain the anomaly through an opposite phase in the kinetic mixing constant.

JHEP10(2019)279

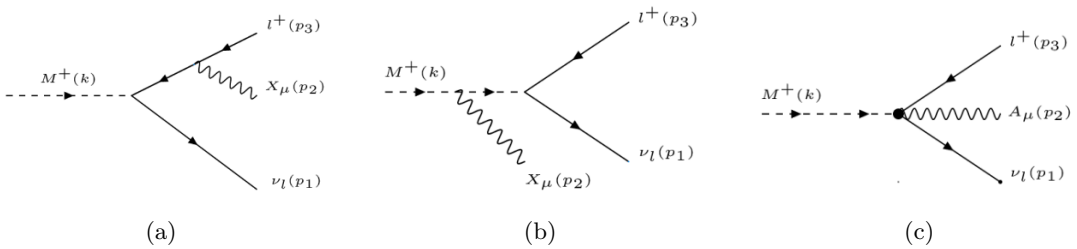

Figure 1. The Feynman diagrams (a,b) contributing to M_{lY}, Y denoting invisibles, in the $\mathrm{U}(1)_X$ model and the structure dependent diagram (c) in QED.

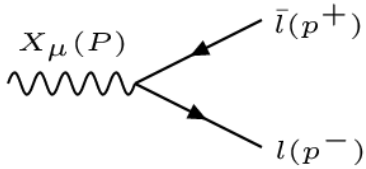

Figure 2. For $m_X < 2m_\mu$ the boson X_μ has five directly decay modes, $l = e, \chi, \nu$.

The details of the decay width calculation are given in appendix B. Assuming that the vector X_μ decays into the invisible pairs $\bar{\chi}\chi, \bar{\nu}\nu$, its contribution to the process $K \to \mu + invisibles$ can be constrained by the existing experimental bound [21]

$$\frac{\Gamma_{K\mu Y}}{\Gamma_{K\mu\nu}} < 3.5 \times 10^{-6}, \qquad 90\% \text{ C.L.}, \tag{3.24}$$

with the missing energy in the interval $227.6 < m_Y(MeV) < 302.2$. The vertex $X_\mu\bar{\chi}\chi$ is extracted from the Lagrangian component

$$\mathcal{L} \supset \frac{g_R}{2} X_\mu \bar{\chi}\gamma_\mu(1+\gamma_5)\chi, \tag{3.25}$$

with g_R given by eq. (2.3c). Since χ_R is a singlet under the SM gauge group and $X_\chi = -1$, it follows that the Feynman's rule for the $X_\mu\bar{\chi}\chi$ is $i(g_X/2)\gamma_\mu(1+\gamma_5)$, where we set $c_\theta \sim 1$. If the mass of X_μ is in the MeV region, the dark boson may still decay into a electron-positron pair, whose vertex is written in eq. (A.2). In the NWA,

$$\begin{aligned}\Gamma_{K\mu Y} &= \Gamma_{K\mu\bar{\chi}\chi} + 3\Gamma_{K\mu\bar{\nu}\nu} \\ &= \frac{1}{3}\Gamma(K \to \mu\nu X)\left[\mathrm{BR}(X \to \chi\bar{\chi}) + 3\mathrm{BR}(X \to \nu\bar{\nu})\right],\end{aligned} \tag{3.26}$$

where the factor of three accounts for the neutrino flavors. The decay amplitude coming from the diagrams in figure 2 can be written most generally as

$$\mathcal{M}_l = \frac{1}{2}\left[\bar{u}(p^-)\gamma_\mu(x_V^l + x_A^l\gamma_5)v(p^+)\right]\epsilon^\mu(P). \tag{3.27}$$

From eq. (3.25), $x_V^\chi = x_A^\chi = g_X$. Again, one can estimate the branching ratio

$$\mathrm{BR}(X \to \bar{a}a) = \frac{\Gamma(X \to \bar{a}a)}{\sum_l \Gamma(X \to \bar{l}l)} \tag{3.28}$$

JHEP10(2019)279

where, from eq. (B.1),

$$\Gamma(X \to \bar{l}l) = \frac{\sum |\mathcal{M}_{X\bar{l}l}|^2}{2m_X} \frac{\Phi_2(X \to \bar{l}l)}{(2\pi)^2}, \tag{3.29}$$

i.e.

$$\mathrm{BR}(X \to \bar{a}a) = \frac{|\mathcal{M}_{X\bar{a}a}|^2 \sqrt{\lambda(m_X^2, m_a^2, m_a^2)}}{\sum_l |\mathcal{M}_{X\bar{l}l}|^2 \sqrt{\lambda(m_X^2, m_l^2, m_l^2)}}. \tag{3.30}$$

The sum over l takes all $l = \chi, e, \nu_e, \nu_\mu, \nu_\tau$. Finally, from the amplitude of eq. (3.27), one can write the general formula

$$|\mathcal{M}_{X\bar{l}l}|^2 = 4\left[2m_l^2\left({x_V^l}^2 - 2{x_A^l}^2\right) + m_X^2\left({x_V^l}^2 + {x_A^l}^2\right)\right], \tag{3.31}$$

where the average over final state spins is made implicit. Since $x_V^\chi = x_A^\chi$, the equation is simplified, such that

$$|\mathcal{M}_{X\bar{\chi}\chi}|^2 \propto [m_X^2 - m_\chi^2] \tag{3.32}$$

i.e. the decay width of $X \to \chi\bar{\chi}$ is suppressed by the difference between X and χ masses. Provided by the experimental constraint [21], we present some examples of the allowed region for $m_X \times g_X^2$ in figure 3 and figure 4.

3.4 $(g-2)_e$

The contribution to the electron anomalous moment a_e, coming from the new dark gauge boson X_μ is equivalent to a shift in the fine-structure constant, as already discussed in ref. [7]

$$d\alpha = 2\pi a_e^X \quad \to \quad \frac{d\alpha^{-1}}{\alpha^{-1}} = -\frac{2\pi a_e^X}{\alpha}. \tag{3.33}$$

The r.h.s. is the relative correction to the measurement of α^{-1} which should not exceed 0.5 ppb [1]. The contribution of the X_μ gauge boson to the electron magnetic moment in the dipole function can be written as

$$a_e^X = \frac{m_e^2}{4\pi^2}\left[(x_V^e)^2 I_V(m_X^2) + (x_A^e)^2 I_A(m_X^2)\right], \tag{3.34}$$

where

$$\begin{aligned} I_V(m_X^2) &= \int_0^1 dz \frac{z^2(1-z)}{[m_l^2 z^2 + m_X^2(1-z)]} \overset{m_X \gg m_l}{\to} \frac{1}{3m_X^2}, \\ I_A(m_X^2) &= \int_0^1 dz \frac{z(1-z)(z-4) - \left(2\frac{m_l^2}{m_X^2}\right) z^3}{[m_l^2 z^2 + m_X^2(1-z)]} \overset{m_X \gg m_l}{\to} -\frac{5}{3m_X^2}. \end{aligned} \tag{3.35}$$

Since the limit $m_X \gg m_e$ is valid in our analysis, we can set the bounding curve

$$f\left(\frac{m_e^2}{m_X^2}\right) \equiv \left(\frac{m_e^2}{m_X^2}\right) \frac{1}{6\pi\alpha} |(x_V^e)^2 - 5(x_A^e)^2| < 0.5\text{ppb} \tag{3.36}$$

JHEP10(2019)279

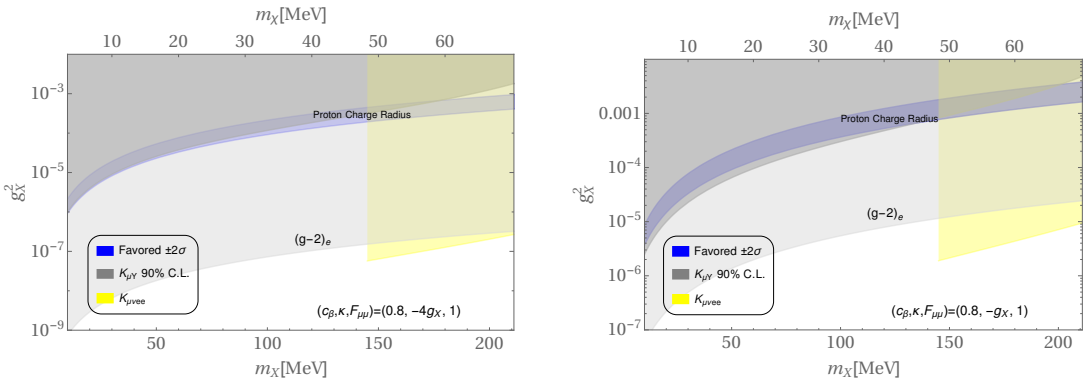

(a) (b)

Figure 3. The allowed region for the proton radius explanation, using the bound in eq. (3.24). Under the narrow-width approximation the vector X_μ decays into the missing $\bar{\chi}\chi, \bar{\nu}\nu$ pairs. Here $m_X = 3m_\chi$ and $\mathbb{F}_{\tau\tau} = 0$.

Parameter space. As discussed in Part I, we have to find out how to fix a plane in a five-dimensional parameter space assuming that the model can explain the selected experimental discrepancies. If we insist to explain the proton charge radius puzzle, one has to require

$$\operatorname{sgn} g_X = -\operatorname{sgn} \kappa. \tag{3.37}$$

In the examples depicted in figure 3, it is evident how stringent are the bounds from $(g-2)_e$. However, due to the interplay of the contributions coming from the vector and axial-vector couplings, the curve can be minimized through the root equation

$$|(x_V^e)^2 - 5(x_A^e)^2| = 0 \tag{3.38}$$

with a fixed $\mathbb{F}$, i.e. around the roots there is almost no effect from the dark boson X to the fine structure constant. If $\mathbb{F}_{ee} = 0$ the solutions to eq. (3.38) are

$$n \in \left[-\frac{7}{5}, \frac{3}{2}, 3\right] c_\beta^2. \tag{3.39}$$

for $\kappa = n g_X$. Due to the condition of eq. (3.37) only $n = -7/5c_\beta^2$ may be a solution for the proton puzzle, as presented in figure 4. We denote $\kappa_0 = -7/5c_\beta^2 g_X$. Note that for κ_0 value, the $(g-2)_e$ bound reduces the discrepancy of the proton puzzle from 5σ to 2σ. In the case where κ is not inside the range of eq. (3.39), then the electron anomalous magnetic moment gives the most stringent bound on the parameter space.

In the following calculations we have written the electron vector and axial-vector couplings to X_μ in the form

$$x_V^e = g_X \left[\frac{g}{c_\phi}\left(2s_\phi^2 - \frac{1}{2}\right)\frac{|2c_\beta^2 - n|}{\bar{g}} + \frac{3n}{2} - \mathbb{F}_{ee}\right], \tag{3.40}$$

$$x_A^e = g_X \left[\frac{g}{2c_\phi}\frac{|2c_\beta^2 - n|}{\bar{g}} + \frac{n}{2} - \mathbb{F}_{ee}\right]. \tag{3.41}$$

In addition, the decay of the vector boson X_μ into neutrino pairs is allowed, with couplings

$$x_V^\nu = -x_A^\nu = \frac{g_X}{2}\left[\frac{g}{c_\phi}\frac{|2c_\beta^2 - n|}{\bar{g}} + n\right]. \tag{3.42}$$

JHEP10(2019)279

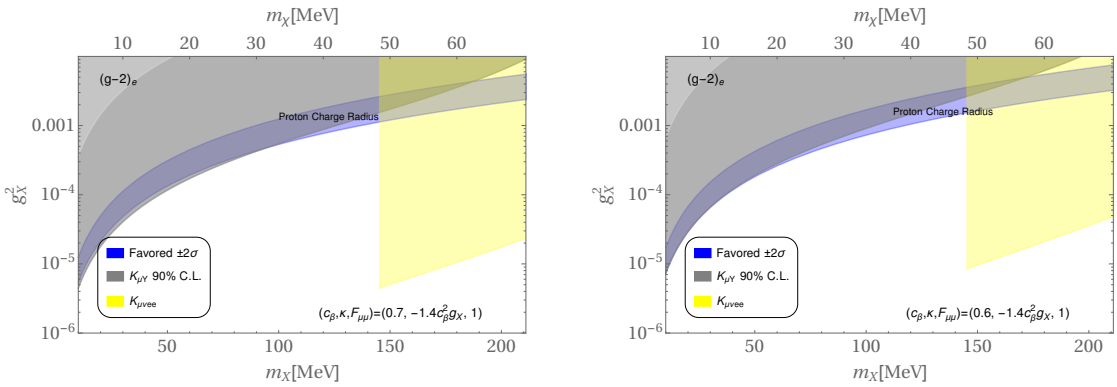

Figure 4. The allowed region for m_X and g_X^2 are presented, when the $(g-2)_e$ curve is minimazed by requiring the cancellation of the vector and axial contributions, as described in the text. Two values of c_β^2 are used. The blue region is allowed by proton anomaly.

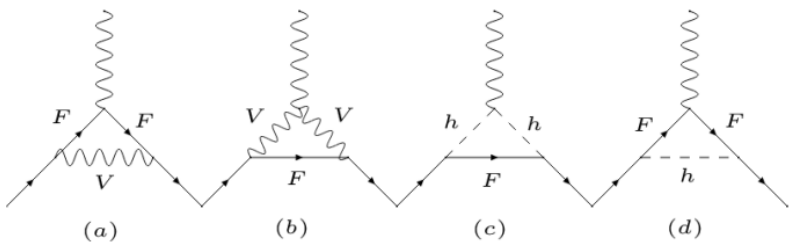

Figure 5. The diagrams contributing to the muon anomalous magnetic moment. The second diagram is not generated in $\mathrm{SM} \otimes \mathrm{U}(1)_X$ theories.

3.5 $(g-2)_\mu$

In figure 5 we present the most general four contributions to the muon anomalous magnetic moment. Since the new vector boson is neutral, the diagram (b) is the only one not contributing to our case. The diagram (c) is present for charged scalars and (d) for neutral Higgs. In this section we want to find the necessary conditions for the correct sign of the $(g-2)_\mu$ discrepancy. In the following, h^+, h^0 generically denote the charged and neutral scalars present in the theory.

Following the work of [22], a general fermion-X_μ vertex can be written as

$$\mathcal{L} = \frac{1}{2}\sum_F \bar{\mu}[x_V\gamma^\rho + x_A\gamma^\rho\gamma^5]F\ X_\rho. \tag{3.43}$$

For simplicity, we do not include the suppressed flavor violating processes, i.e. $F=\mu$. For $m_F = m_\mu$, the integral linked to the first diagram is given by

$$[a_\mu]_a = \frac{m_\mu^2}{16\pi^2}\int_0^1 dz\ \frac{\left[x_V^2[(z-z^2)z] + x_A^2[(z-z^2)(z-4) - 2\frac{m_\mu^2}{m_X^2}z^3]\right]}{m_\mu^2 x^2 + m_X^2(1-x)}. \tag{3.44}$$

As mentioned before, we work under the assumption of very large Higgs masses, where a_μ is dominated by $[a_\mu]_a$. On the other hand, the above integral leads to a wrong negative sign

JHEP10(2019)279

for a wide range of the c_β parameter, and have to be compensated by additional contributions. Therefore, we assume that scalar masses are relatively large and compute the scalars contributions to the moment function in the region where the asymptotic approximation to the integrals is fairly valid, i.e. $m_h > 20\, m_\mu$. The bounds on the Higgses couplings to Z are coming from the LHC analyses, as already considered by the authors of ref. [23]. The Yukawa Lagrangian can be parametrized as

$$\mathcal{L}_Y = \sum_{h,F} \bar{\mu}[C_S + C_P\gamma_5]F\ h. \tag{3.45}$$

Both diagrams (c) and (d) can contribute to the muon anomalous magnetic moment. For the diagram(c) we have to specify $F = \nu$ or $m_F = 0$. The coupling C_P is in fact present in our model for both neutral and charged scalars and, in the neutral case, it is purely imaginary. For $m_F = m_\nu = 0$ it follows that

$$[a_\mu]_c = \frac{m_\mu^2}{8\pi^2}(|C_S^+|^2 + |C_P^+|^2)\int_0^1 dz \frac{(z^3 - z^2)}{m_\mu^2 z^2 + m_{h^+}^2(1-z)} \tag{3.46}$$

and for neutral scalars in the diagram (d) $F = \mu$, one gets

$$[a_\mu]_d = \frac{m_\mu^2}{8\pi^2}\int_0^1 dz \frac{|C_S^0|^2(2z^2 - z^3) + |C_P^0|^2 z^3}{m_\mu^2 z^2 + m_{h^+}^2(1-z)}, \tag{3.47}$$

with

$$(g-2)_\mu = [a_\mu]_a + [a_\mu]_b + [a_\mu]_c + [a_\mu]_d. \tag{3.48}$$

If we consider $m_{h^+}, m_{h^0} \gg m_\mu$ the integrals converges to a simplified form:

$$[a_\mu]_c \to \frac{m_\mu^2}{8\pi^2}(|C_S^+|^2 + |C_P^+|^2)\left(-\frac{1}{3}\right), \tag{3.49}$$

$$[a_\mu]_d^S \to \frac{m_\mu^2}{m_{h_0}^2}\frac{|C^0|_S^2}{8\pi^2}\left[\log\left[\frac{m_{h_0}^2}{m_\mu^2}\right] - \frac{7}{6}\right], \tag{3.50}$$

$$[a_\mu]_d^P \to \frac{m_\mu^2}{m_{h_0}^2}\frac{|C^0|_P^2}{8\pi^2}\left[\log\left[\frac{m_{h_0}^2}{m_\mu^2}\right] - \frac{11}{6}\right]. \tag{3.51}$$

Therefore, the charged scalars cannot provide the correct sign and their interactions have to be suppressed, either by their large masses or by their negligible couplings to muons. In summary, in order to explain the $(g-2)_\mu$ discrepancy only diagram (a) and (d) contribute. Again, there is a range for c_β in which the (a) integral already gives the correct sign for the a_μ discrepancy, allowing all the scalars to live in the decoupling limit. For instance, if we do not take into account the constraint coming from the proton radius, then we can use all solutions derived from eq. (3.39). Thus, for $\kappa = \frac{3}{2}c_\beta^2 g_X$, and $c_\beta < 0.9$, light neutral scalars with masses in the range $m_{h^0} \in (10 - 100)m_\mu$ are required to restore $(g-2)_\mu$, for $|C^0|_S \sim |C^0|_P \sim 10 g_X$ and different values for c_β. Charged scalars are still disfavored. Since $c_\beta^2 = v_X^2/v^2$, a minimal model at low-energies (MeV) is well supported by a small scale v_X. For the completeness of our study, let us mention that the pairs $\kappa = -\frac{7}{5}c_\beta^2 g_X$ and $c_\beta > 0.7$, as well as $\kappa = 3c_\beta^2 g_X$ and $c_\beta > 0.99$, both can solve, through (a) diagram only, the discrepancy of $(g-2)_\mu$.

JHEP10(2019)279

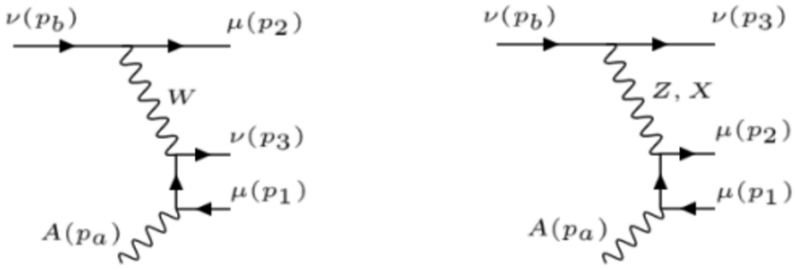

Figure 6. The trident production in the equivalent photon approximation (EPA). In addition, there are the reciprocal diagrams where the real photon is attached to μ^-.

3.6 $K_{\mu\nu e^+e^-}$

The decay width of $K_{\mu\nu e^+e^-}$, denoted as $\Gamma_{K\mu 2ee}$, is obtained from the distribution $\frac{d\Gamma_{K\mu 2ee}}{dm_{ee}}$, integrated over the electron-positron invariant mass $m_{ee} > 145$MeV [15]. We use the narrow-width approximation in a way that, for a fixed $m_X = m_{ee}$, the contribution from $X \to ee$ should not exceed the uncertainty of the total $\Gamma_{K\mu 2ee}$. By demanding that the decay rate has to be smaller than the experimental uncertainty, it actually implies that no enhancement should be seen in the region $m_{ee} > 145\,\text{MeV}$. The analysis is similar to the calculation of $\Gamma_{K\mu Y}$, now with

$$\frac{1}{3}\frac{\Gamma(K \to \mu\nu_\mu X)}{\Gamma_K}\text{BR}(X \to e^+e^-) < 3.1 \times 10^{-9}, \tag{3.52}$$

for $145\,\text{MeV} < m_X < 2m_\mu$. In figure 3 and figure 4 the excluded region is marked by the yellow color.

3.7 Neutrino trident production

We determine the cross-section for the neutrino trident production in the Equivalent Photon Approximation (EPA) [3, 24–26], i.e. by connecting it with the scattering of a real photon and the neutrino beam. We then include the bound from the CHARM-II experiment [27].

The total amplitude for the scattering of a real photon and a neutrino beam in $\gamma\nu \to \nu\mu^+\mu^-$ includes the six diagrams of figure 6 for the exchange of W, Z and X bosons. The neutrinos spins are summed, while one takes the average over the photon polarization, i.e.

$$\frac{1}{2}\sum_p |\mathcal{M}|^2 = -\frac{1}{2}[\mathcal{M}]^\alpha[\mathcal{M}]^*_\alpha. \tag{3.53}$$

In the case of the neutral currents, both Z and X, the neutrino vector and axial-couplings are related by

$$x_V^\nu(z) = -x_A^\nu(z) \equiv x_z^\nu, \tag{3.54}$$

where $z = Z, X$. The amplitude can be simplified and presented as

$$[\mathcal{M}]^\alpha = \frac{G_F}{\sqrt{2}}e[\overline{u}_\nu(k_2)\gamma_\nu(1-\gamma_5)u_\nu(k_1)]\mathcal{F}^{\alpha\nu}, \tag{3.55}$$

JHEP10(2019)279

with

$$\mathcal{F}^{\alpha\nu} = B_-[\overline{u}_\mu(p_-)\gamma^\alpha\{(\not{p}_- - \not{q}) + m_\mu\}\gamma^\nu(C_V + C_A\gamma_5)v_\mu(p_+)] \\ +B_+[\overline{u}_\mu(p_-)\gamma^\nu(C_V + C_A\gamma_5)\{(\not{q} - \not{p}_+) + m_\mu\}\gamma^\alpha v_\mu(p_+)] \tag{3.56}$$

and $B_i \equiv [(p_i - q)^2 - m_\mu^2]^{-1}$. The constants $C_{V,A}$ summarize the contributions coming from all diagrams

$$C_V = \sum_{z=Z,X} \frac{x_z^\nu x_V^\mu(z)}{2\sqrt{2}G_F}[k^2 - m_z^2]^{-1} - 1, \qquad C_A = \sum_{z=Z,X} \frac{x_z^\nu x_A^\mu(z)}{2\sqrt{2}G_F}[k^2 - m_z^2]^{-1} + 1. \tag{3.57}$$

These expressions are exact in the sense that the Z mass parameter depends on the new g_X, s_θ. Once the vertices are defined as in eq. (2.9), by taking $c_\theta \approx 1$ and neglecting second order terms on the small parameters, the SM contribution to neutrino trident production is given by

$$C_V^{\rm SM} = -\left(\frac{1}{2} + 2s_\phi^2\right), \qquad C_A^{\rm SM} = \frac{1}{2}. \tag{3.58}$$

The phase-space for the scattering of a real photon and a neutrino can be defined through the invariants [28] (see figure 6)

$$s_1 = (p_1 + p_2)^2, \quad t_1 = (p_a - p_1)^2, \quad s_2 = (p_2 + p_3)^2, \quad t_2 = (p_a - p_1 - p_2)^2. \tag{3.59}$$

In the EPA, the total cross-section can be written as [29]

$$\sigma(\nu N \to \nu N \mu^+\mu^-) = \frac{Z^2e^2}{64\pi}\frac{1}{(2\pi)^5}\int_{\frac{2m_\mu^2}{E_\nu}}^{\infty} dq \int_{4m_\mu^2}^{2E_\nu q} ds \int_{(m_2+m_3)^2}^{(\sqrt{s}-m_1)^2} ds_2 \int_{t_1^-}^{t_1^+} dt_1 \int_{t_2^-}^{t_2^+} dt_2 \\ \cdot \int_0^{2\pi} d\phi \frac{F^2(q^2)|\mathcal{M}|^2}{qs^2\lambda^{1/2}(s, m_1^2, m_b^2)\lambda^{1/2}(s_2, m_b^2, t_1)}, \tag{3.60}$$

where $q \equiv |q|$, Z is the atomic number of the target and $F(q^2)$ is the electromagnetic form-factor introduced in [3, 29]. The details of the integration over phase space are given in appendix B. In eq. (3.60) the integrals over q (with $q \equiv \sqrt{q^2}$) and $s = (p_a + p_b)^2$ are derived from the probability of creating a virtual photon with momenta q, defined by [3]

$$P(q^2, s) = \frac{Z^2e^2}{4\pi^2}\frac{ds}{s}\frac{dq^2}{q^2}F^2(q^2) \tag{3.61}$$

and the electromagnetic form factor $F(q^2) = \left[1 + 1.21\frac{q^2}{m_p^2}\right]^{-2}$ is given in ref. [24], where m_p is the proton mass. In the CHARM-II experiment, a neutrino beam with the mean energy $E_\nu \sim 20\,\text{GeV}$ is scattered by a glass target ($Z = 10$). We require that the contribution coming from the interference of the SM and the SM $\otimes$ U(1)$_X$ to the total cross-section should be inside the one standard deviation region, i.e.

$$|\sigma_{\rm SM+X}^{\rm int}| < 0.57\,\sigma_{\rm SM}. \tag{3.62}$$

For the SM prediction, averaged over both neutrino and antineutrino scattering, we obtained $\sigma_{\rm SM} = 1.8 \times 10^{-41}\text{cm}^2$.

JHEP10(2019)279

3.8 χ relic abundance

In this section we compute the relic abundance for a thermally produced χ-fermion from a set of fixed points in the parameter space. Before we proceed to the details, it is important to emphasize that our computation will follow the standard scenario presented in [14]. Since Cold WIMPs freeze-out in the pre-Big Bang Nucleosynthesis (BBN) epoch, the results rely on a number of assumptions concerning the early history of the universe during an interval from which no information can be collected. Therefore, they may substantially differ between independent cosmological models. These assumptions are commonly centered, for instance, on the expansion rate of the universe at the freeze-out, the kinetic and chemical equilibrium state before the decoupling, and on the dominant interactions for the WIMP production in the plasma, if thermally produced [30]. In the following, we set up the framework which determines a bounding curve to the χ parameters, in accordance with the current measurement of $\Omega_{\rm CDM}$.

We start with the exact solution of the Boltzmann equation, aiming to examine the sensitivity of the allowed band on small variations of the couplings. We then consider the approximate formula for the weakly interacting massive particles (WIMP) relic density [30]

$$\Omega h^2 \approx \frac{3\times 10^{-27}{\rm cm}^3 s^{-1}}{\langle \sigma_{\rm ann} v\rangle}. \tag{3.63}$$

with the thermal average computed at the freeze-out temperature $T_{f.o.} \backsimeq \frac{m_\chi}{20}$. In the general case, the attempt to create a direct bounding curve (i.e. $g_X < f(m_X^2)$ for the analytical function f) is difficult due to the presence of the X boson as a resonance. In other words, the coupling g_X cannot be easily factorized, once it enters the decay width in the Breit-Wigner propagator. We perform the integration of

$$\frac{dY}{dx} = -\left(\frac{45}{\pi M_P^2}\right)^{-1/2} \frac{g_*^{1/2} m_\chi}{x^2}\langle\sigma v\rangle (Y^2 - Y_{\rm eq}^2), \tag{3.64}$$

by describing the evolution of the comoving abundance Y, whose value at chemical equilibrium is given by [14]

$$Y_{\rm eq} = \frac{45g}{4\pi^2}\frac{x^2 k_2(x)}{h_{\rm eff}(m/x)}. \tag{3.65}$$

Above, the $M_P = 1.22\times 10^{19}$GeV is the Planck mass. The variable $x \equiv \frac{m_\chi}{T}$, where T is the photon temperature. It is commonly taken from $x = 1$, which defines the boundary for the condition $Y = Y_{\rm eq}$, to the present value. According to ref. [14], we choose for the χ mass range, $10\,{\rm MeV} < m_\chi < 80\,{\rm MeV}$, such that the effective degrees of freedom $g_*^{1/2}$ has a small deviation from $g_*^{1/2} \approx 7/2$ due to QCD quark-hadron phase transition, which we neglect in our calculation. In eq. (3.65), the constant g accounts the degrees of freedom for the particles present at the equilibrium. We consider the dominant channels including ν, e, μ, χ. On the other hand, the $h_{\rm eff}(T)$ encloses the effective degrees of freedom for entropy and, in principle, it should sum over all species present in the plasma. In practice, however, the

JHEP10(2019)279

species with large energies are suppressed by their distribution function such that we may sum over photons in addition to the particles at the equilibrium.[4]

The thermally averaged annihilation cross-section is regulated by the diagram of figure 10 with $\chi\bar{\chi}$ in the initial states and f summed over the particles at chemical equilibrium. Co-annihilations are discarded. The expression for $\langle\sigma v\rangle$ can be written as [14]

$$\langle\sigma v\rangle = \frac{x}{8m_\chi^5 k_2^2(x)} \int_{4m_\chi^2}^{\infty} ds \left[\sqrt{s}(s-4m_\chi^2)k_1\left(x\frac{\sqrt{s}}{m_\chi}\right)\sigma\right], \tag{3.67}$$

where, as in eq. (3.65), the k_i are the order i modified Bessel functions. The cross-section σ is a sum over f such that

$$d\sigma_f = \frac{d\Omega}{64\pi^2}\frac{(s-4m_f^2)^{1/2}}{(s-4m_\chi^2)^{1/2}}\frac{\frac{1}{4}|\mathcal{M}_{\chi\bar{\chi}\to f\bar{f}}|^2}{s} \tag{3.68}$$

is the differential cross section for each fermion f in the final state. Again, the X_μ resonance is dominant over the remaining mediators and is implemented as a Breit-Wigner vector whose χ couplings are $x_V^\chi = x_A^\chi = g_X$. The total amplitude squared can be integrated over the polar angle and results in the expression

$$\int d\theta|\mathcal{M}|^2 = g_X^4 \frac{8m_\chi^2\left[m_f^2(35{x_A^f}^2+29{x_V^f}^2)-8s({x_A^f}^2+{x_V^f}^2)\right]+19s{x_A^f}^2(s-4m_f^2)+s{x_V^f}^2(19s-52m_f^2)}{3(\Gamma_X^2 m_X^2+(m_X^2-s)^2)}. \tag{3.69}$$

The solution of eq. (3.64) then has to be translated in the present time. The abundance Y_0 is related to the WIMP relic density through [30]

$$\Omega_\chi h^2 = 2.755\times 10^5 Y_0 \frac{m_\chi}{\text{MeV}} \tag{3.70}$$

and must be consistent with the current measurement $\Omega_{\text{CDM}}h^2 = 0.1131(34)$ [31] of the cold dark matter density. In figure 7(a) we present the integrand of the thermal average in eq. (3.67) for different temperatures, under a fixed point in the parameter space, dominated by the resonance.[5] In figure 7(b) we present the solution of eq. (3.64) for the WIMP mass $m_\chi = 30\,\text{MeV}$, $g_X = 4\times 10^{-3}$ and a set of couplings x. It depicts the point where the low temperatures hinder the abundance to follow the evolution of its equilibrium value, and the particle decouples. The horizontal black band is the 3σ limit for the current relic abundance. The well-known pattern of the figure 7(b) reveals that the relic density gets

[4]The relevant species are considered to be at thermal equilibrium with the plasma and $h_{\text{eff}}(T) = \sum_i h_i(T)$ where

$$h_i(T) = \frac{90g_i}{(2\pi)^5T^3}\int \frac{3m_i^2+4p_i^2}{3E_iT}\frac{p_i^2dp_i}{\exp E_i/T+\eta_i}, \tag{3.66}$$

g_i accounts the number of spin degrees of freedom of i, while E_i, m_i and $\eta_i = 1(-1)$ denote its energy, mass and Fermi-Dirac (Bose-Einstein) statistics, respectively.

[5]The numerical integration can be optimized by hiding the pole via the approximation

$$\int_\alpha^\infty f(x)dx \approx \int_\alpha^{x_p-\epsilon} f(x)dx + \int_{x_p+\epsilon}^\infty f(x)dx + \epsilon[f(x_p)+f(x_p-\epsilon)], \tag{3.71}$$

for a Breit-Wigner function whose pole is $x_p \gg \epsilon$.

JHEP10(2019)279

overabundant for small couplings, a feature that will help us to maximize the excluded region of our parameter space. Although an underabundant sector is disfavored by $\Omega_{\rm CDM}$, it actually informs us about the necessity of completing the theory with additional dark matter candidates, and is not entirely ruled out. One can also notice from the figure how sensitive Y_0 is to small variations of g_X. We consider that the use of eq. (3.63) is appropriate for our precision level, and it may simplify our analysis. For large temperatures ($x < 20$) and small couplings ($g_X \lesssim 10^{-2}$, $c_\beta \in [0.4, 0.95]$) the integral is dominated by the region around the resonance and is sufficiently narrow to use a Dirac delta approximation.[6] In order to illustrate the importance of the relation between the X_μ and χ fermion masses, in figure 8(a) we present the favored band for the current relic abundance by taking the relation $m_X = y m_\chi$ for different values of y, at the freeze out temperature $x_{f.o.} = 20$. In figure 8(b) a similar set of lines is computed for particular choices of c_β.

4 Outlook

The results of the previous section, for two fixed points, were summarized in figure 9. In plot (a), $c_\beta = 0.6$ cannot resolve the $(g-2)_\mu$ discrepancy. Notwithstanding, we can verify the impact of the axial-vector couplings interference in the cross-section of the neutrino trident production (dark-blue region) in comparison with the dark photon case (light-blue). Moreover, the choice of the parameter $\kappa = \frac{3}{2} c_\beta^2 g_X$ renders irrelevant the bound coming from $(g-2)_e$. In plot (b) the favored region for the explanation of the $(g-2)_\mu$ discrepancy (in gray) is presented, for $c_\beta = 0.95$, while the circled area highlight the overlap between the solution for the muon anomaly and the relic abundance $\Omega_{\rm CDM}$ favored bands. The parameter space that we covered hitherto should be further tested. In the following subsection 4.1, we consider the forward-backward asymmetry in electron-positron collision to fermion anti-fermion, $e^+e^- \to \bar{f}f$, in order to determine how the observable is sensitive on the SM $\otimes$ U(1)$_X$ parameters. Finally, in subsection 4.2 we illustrate the impact of one set of parameters, allowed by figure 9(b), to the leptonic decays $M \to j\nu_j i^+ i^-$, where $M = \pi, K, D, D_s, B$ and $i, j = e, \mu$.

4.1 Parity non-conserving observables

Light Z' physics requires the use of the LEP data, where the effects of Z interactions are suppressed by its large mass. Here, we have to constrain the region for the light Z' and its small couplings. As we mentioned in the previous section, in scattering processes, the dark photon effects can be considered as a correction to the fine-structure constant. When the axial-vector coupling of the dark gauge boson is present it can be tested in the angular asymmetries of the differential cross-section. The forward-backward asymmetry is defined as

$$A(\theta) \equiv \frac{d\sigma(\theta) - d\sigma(\pi-\theta)}{d\sigma(\theta) + d\sigma(\pi-\theta)}. \tag{4.1}$$

[6] I.e. we replace the Breit-Wigner propagator by

$$\frac{1}{(s-m_X^2)^2 + (m_X\Gamma_X)^2} \to \frac{\pi}{m_X\Gamma_X}\delta(s-m_X^2) \tag{3.72}$$

JHEP10(2019)279

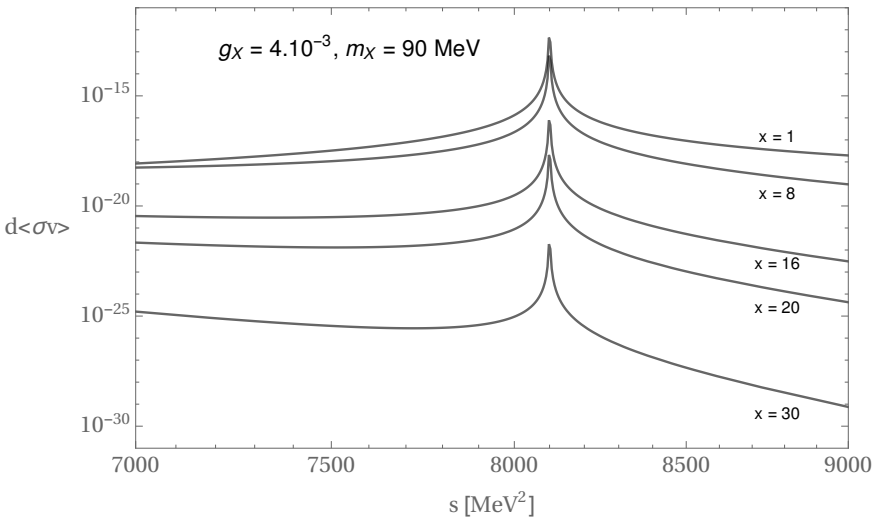

(a)

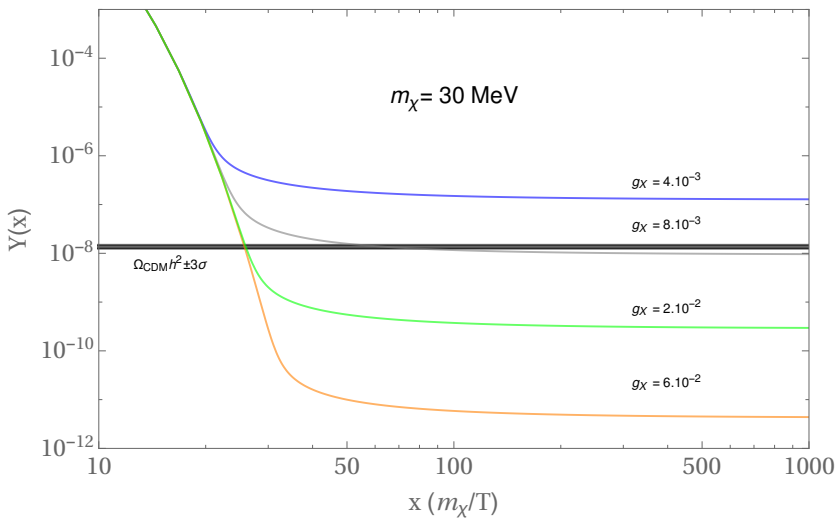

(b)

Figure 7. (a) The differential thermal average dominated by a narrow resonance. In the example, the X boson mass is $m_X = 90\,\text{MeV}$, while the dark fermion mass is $m_\chi = 30\,\text{MeV}$. In (b), the horizontal black band presents the 3σ region allowed by the current measurement of cold dark matter density. The abundance Y_0 is sensitive to small variations of the coupling constant g_X, such that Ω_{CDM} provides a strong bound for $\text{SM} \otimes \text{U}(1)_X$ theories. The remaining parameters are fixed as $(c_\beta, \kappa, F_{\mu\mu}) = (0.6, 1.5c_\beta^2 g_X, 1)$.

Here we will focus on the energy region far from both Z and X peaks, i.e. $2m_\mu \ll \sqrt{s} \ll m_Z$ and we must compute the generic diagram in figure 10 for $V = \gamma, Z, X$. For simplicity, the Feynman rule for the vertex $\bar{f} f V_\mu$ can be written as $ie\gamma_\mu(v_f^V - a_f^V \gamma_5)$. For instance, $(v_f^\gamma, a_f^\gamma) = (-q_f, 0)$ where $q_e = -1, q_u = \frac{2}{3}, q_d = -\frac{1}{3}$. The amplitude can be expressed as

$$\mathcal{M}_V = \frac{e^2}{s - m_V^2}[\bar{v}(p^+)\gamma^\mu(v_e^V - a_e^V\gamma_5)u(p^-)][\bar{u}(k^-)\gamma_\mu(v_f^V - a_f^V\gamma_5)v(k^+)], \tag{4.2}$$

JHEP10(2019)279

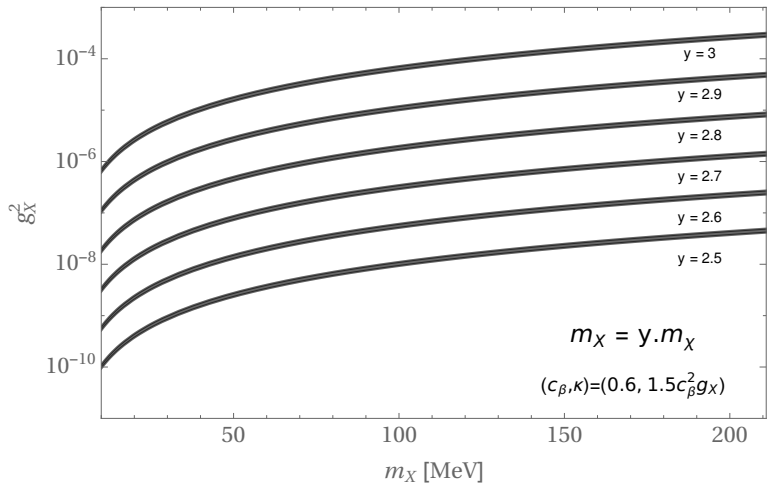

(a)

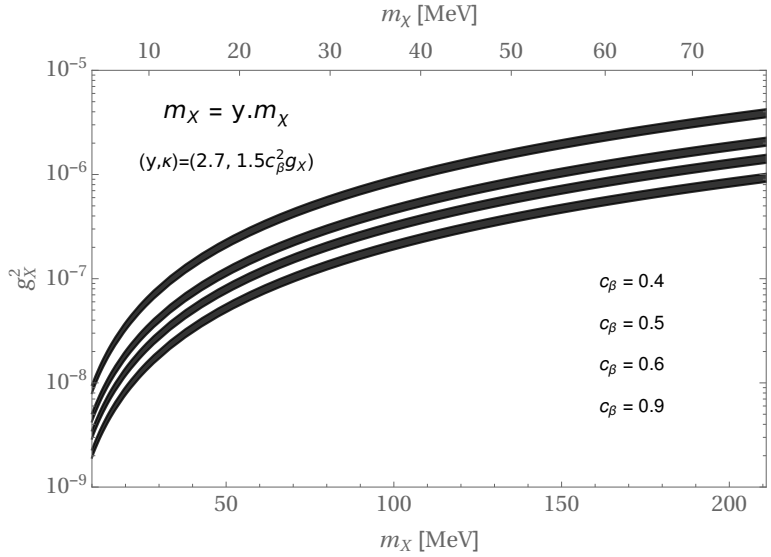

(b)

Figure 8. The 3σ favored region for $\Omega_{\rm CDM}h^2$. In (a) it is illustrated how the variations in the relation $m_X = ym_\chi$ move the allowed region. In (b), the lines are less sensitive under small variations of c_β. The region below each line corresponds to overabundant $\Omega_\chi h^2$.

with $|\mathcal{M}|^2 = |\sum_{V=\gamma,Z,X} \mathcal{M}_V|^2$. The dominant contribution to $A(\theta)$ originates from the interference of contributions coming from γZ and γX in the numerator, while the cross section coming from the photon mediator (γ) gives the dominant contribution in the denominator, i.e.

$$A(\theta) \approx \frac{[d\sigma^{\gamma Z}(\theta) + d\sigma^{\gamma X}(\theta)] - [d\sigma^{\gamma Z}(\pi-\theta) + d\sigma^{\gamma X}(\pi-\theta)]}{d\sigma^{\gamma}(\theta) + d\sigma^{\gamma}(\pi-\theta)}. \tag{4.3}$$

In the CM reference frame it results in

$$A(\theta) \approx \frac{8sc_\theta|\mathbf{k}|\sqrt{s}}{4c_\theta^2|\mathbf{k}|^2 + 4m_f^2 + s}\left[\frac{a_e^X a_f^X}{s-m_X^2} + \frac{a_e^Z a_f^Z}{s-m_Z^2}\right]. \tag{4.4}$$

JHEP10(2019)279

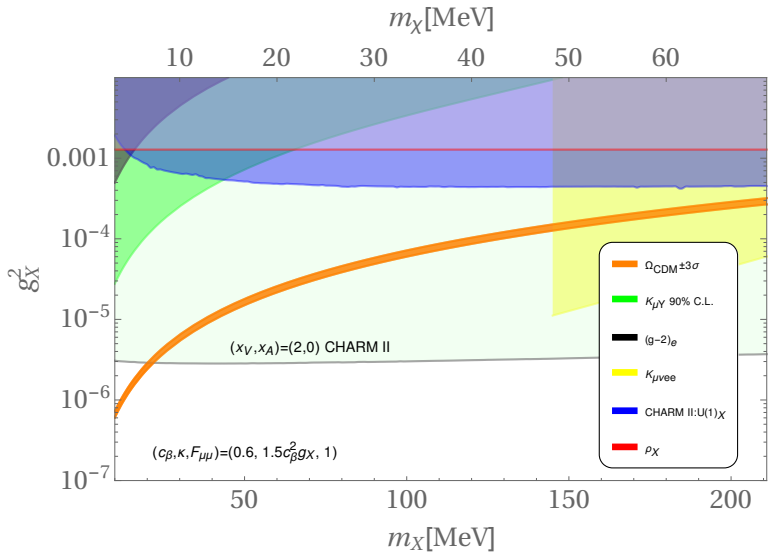

(a)

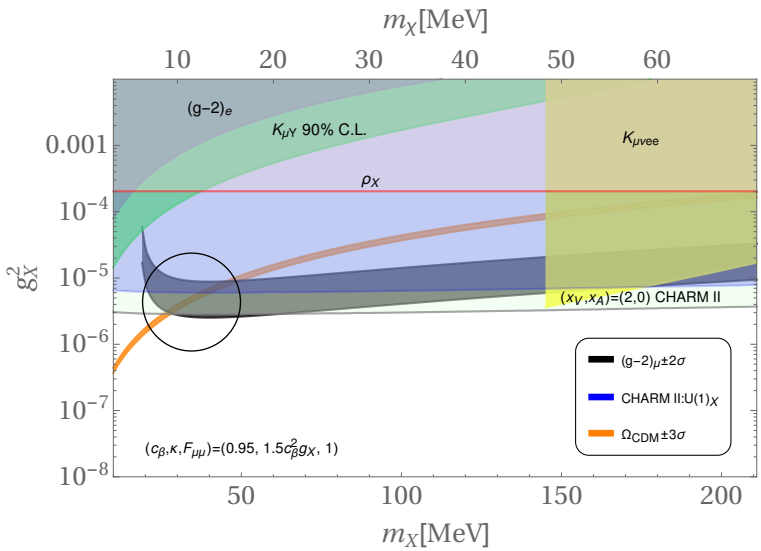

(b)

Figure 9. The parameter space for $\kappa = \frac{3}{2}c_\beta^2 g_X$. Notice, in (a), the excluded region for the dark photon (A')(light-blue) is presented in comparison to the dark gauge boson (Z') region (dark-blue). In (b), the difference is reduced when $c_\beta = 0.95$ which, on the other hand, produces a possible solution both for the $(g-2)_\mu$ discrepancy and the $\Omega_{\rm CDM}$ (circled region).

Here c_θ is the scattering angle, and $\mathbf{k}$ the space-momentum of the particles in the final state. In the region $\sqrt{s} \gg m_\mu$ the contribution coming from X exchange can be written as $\delta A^X(\theta) \propto \frac{a_e^X a_f^X}{s}$ or

$$A(\theta) \propto \left[\frac{a_e^X a_f^X}{s} - \frac{a_e^Z a_f^Z}{m_Z^2}\right]. \tag{4.5}$$

JHEP10(2019)279

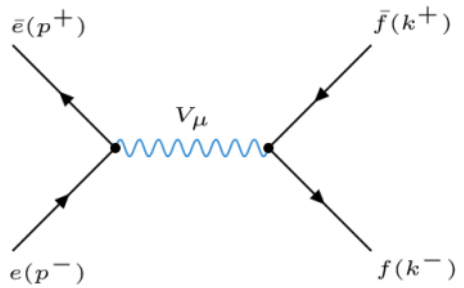

Figure 10. Forward-backward asymmetries in $e^+e^- \to \bar{f}f$ are important tests for axial-vector couplings. The model predict non-universality for $f = \mu$ and $f = \tau$. Here $V = \gamma, Z, X$.

In our case, by assuming $a^Z \sim g$ and $a^X \sim g_X$, the region around $\sqrt{s} \sim \frac{m_Z}{10}$ would severely constrain $g_X \sim 10^{-1} g$. In summary, the precise measurement of forward-backward asymmetry, in the region described above, might provide an additional limit to the coupling g_X, as well as a possible test of lepton-flavor universality.

4.2 Leptonic meson decays: $M \to l'\nu_{l'}ll$

The experimental measurement of the branching ratio for $K_{\mu\nu ee}$ gives the most stringent bound of figure (9). This result motivates us to extrapolate this analysis and make predictions for the bottom and charm mesons. In this section we present our results for the total and differential branching ratio of the purely leptonic decays $M \to l'\nu_{l'}l^+l^-$, or simply $M_{l'2ll}$, where M denotes the mesons $M = \pi, K, D, D_s, B$ and $l', l = e, \mu$. The diagrams in figure 1 are dominant in that process and can be separated into the inner-bremsstrahlung (IB) amplitude (a,b) and a structure dependent (SD) amplitude (c). The off-shell vectors X_μ, A_μ mediate the interaction with the lepton pair l^+l^-. The IB amplitudes can be computed in a general form for all mesons by following the work of [32]. The SD diagram can be parametrized as

$$\mathcal{M}_{SD} = e^2 \frac{G_F}{\sqrt{2}} V^*_{\rm UD} h_{\mu\alpha} [\overline{u}_\nu \gamma^\mu (1-\gamma_5) v_{l'}][\overline{u}_i l \gamma^\alpha v_l], \tag{4.6}$$

where $V_{\rm UD}$ is the CKM element linked to the particular meson's quark structure, and

$$h_{\mu\alpha} = \frac{1}{p^2}\left[\epsilon_{\mu\alpha\lambda\beta} k^\lambda p^\beta \frac{F_V(p^2)}{m_M} - ie\left(g_{\mu\alpha} p\cdot(k-p) - p_\mu (k-p)_\alpha\right)\frac{F_A(p^2)}{m_M}\right]. \tag{4.7}$$

In general, the IB contribution is dominant in $M_{\mu 2ee}$ and suppressed in $M_{e2\mu\mu}$. We compute the differential branching ratio for D_s decay, in the SM framework, including both IB + SD interference. The form-factors are given by:[7]

$$F_V(p^2) = \frac{0.029}{1 - \frac{p^2}{(2.11\,GeV)^2}}, \qquad F_A(p^2) = \frac{0.173}{1 - \frac{p^2}{(2.46\,GeV)^2}}. \tag{4.8}$$

In figure 11 we plot the results for different mesons, keeping IB contributions only. The results are summarized in table 1. We provide cuts on the di-lepton invariant mass in order

[7]We acknowledge D. Melikhov for providing us with these form-factors.

JHEP10(2019)279

to connect them to possible experimental limitations. These results for the SM branching ratio might be interesting if precision measurements are reached. In figure 11(b) we present the results for the D_s meson including the SD part. In these last examples, the di-leptons are the e^+e^- and $\mu^+\mu^-$ pairs and the integrated values are presented in table 2.

We also compute the branching ratios for $M_{\mu 2ee}$ ($M = \pi$, K, D, B), coming from the dominant IB amplitudes, in which the photon mixes with the X boson. The branching ratios below test our IB formulas in the SM $\otimes$ U(1)$_X$ framework for the point of figure 12, namely $(g_X^2, m_X) = (4 \times 10^{-4}, 60)$:

$$\begin{aligned} \mathrm{BR}(\pi_{\mu 2ee})_{\mathrm{IBX}} &= 3.27 \times 10^{-7}, \quad \mathrm{BR}(K_{\mu 2ee})_{\mathrm{IBX}} = 2.49 \times 10^{-5}, \\ \mathrm{BR}(D_{\mu 2ee})_{\mathrm{IBX}} &= 6.54 \times 10^{-8}, \quad \mathrm{BR}(B_{\mu 2ee})_{\mathrm{IBX}} = 1.78 \times 10^{-10}, \end{aligned} \tag{4.9}$$

Once more, the increase in the differential branching ratios is tinny and it can eventually be observed if high precision measurements are performed.

In order to provide a possible test for lepton flavor universality we introduce

$$R(f) = \frac{\mathrm{BR}(M_{f2\mu\mu})}{\mathrm{BR}(M_{f2ee})}, \tag{4.10}$$

in a kinematic region far from resonances. In the SM the ratio is close to the unity for $q^2 \gg (2m_\mu)^2$ and different leptons in the final state. This case might be potentially interesting, and it is kinetically allowed only for $B_{\tau 2ll}$. For m_{ll}^2 far from the X_μ pole, any non-universality effects are negligible if compared with the SM prediction. For instance, from the parameters selected for the analysis presented in figure 12, and $(1500)^2\,\mathrm{MeV}^2 < m_{ll}^2 < (1600)^2\,\mathrm{MeV}^2$, we find

$$R_X(\tau) = \begin{matrix} 0.93 & m_X = 1550 \text{ MeV}, \\ 0.99 & m_X = 60 \text{ MeV}, \end{matrix} \tag{4.11}$$

while for the SM value, $R_{\mathrm{SM}}(\tau) = 0.9998$. In the region where the invariant mass of the di-lepton pair is in $(300)^2\,\mathrm{MeV}^2 < m_{ll}^2 < (400)^2\ \mathrm{MeV}^2$ we find

$$R_{\mathrm{SM}}(\tau) = 0.933, \qquad R_X(\tau) = \begin{matrix} 0.90 & m_X = 350 \text{ MeV}, \\ 0.931 & m_X = 60 \text{ MeV}. \end{matrix} \tag{4.12}$$

Finally, in figure 12 we present the normalized differential branching ratio for $Ds_{\mu 2ee}$, both in the SM$\otimes$U(1)$_X$ and in the SM frameworks. Around the resonance, the probability for measuring the di-lepton mass in the interval 58 MeV $< m_{ee} <$ 62 MeV is equal to $P = 2.54\%$, for $(g_X^2, m_X) = (4 \cdot 10^{-4}, 60)$, allowed by figure 9(a), in comparison with $P = 0.63\%$, in the SM.

5 Conclusion

We have explored a number of processes at low energies (MeV-GeV) in order to constrain a SM $\otimes$ U(1)$_X$ theory, UV-completed by cold WIMPs and whose U(1)$_X$ is chiral for right-handed fermions. The most stringent bounds are obtained from the electron anomalous magnetic moment and the neutrino trident production. Dark photons, as U(1)$_X$ gauge

JHEP10(2019)279

$M_{\mu 2ee}$	Full	$m_{ee} \geqslant 0.1 m_M$	$m_{ee} \geqslant 20$MeV	$m_{ee} \geqslant 140$MeV
$\pi_{\mu 2ee}$	3.27×10^{-7}	2.82×10^{-9}	–	–
$K_{\mu 2ee}$	2.48×10^{-5}	8.6×10^{-7}	3.15×10^{-6}	4.97×10^{-8}
$D_{\mu 2ee}$	6.45×10^{-8}	1.13×10^{-9}	1.45×10^{-8}	1.84×10^{-9}
$B_{\mu 2ee}$	1.66×10^{-10}	1.64×10^{-12}	4.69×10^{-11}	1.02×10^{-11}

Table 1. In the SM framework, a set of cuts in the di-lepton mass for the BR($M_{\mu 2ee}$), used in the decay width calculations for IB contributions.

M_{f2ll}	Full	$m_{ll} \geqslant 0.1 m_{Ds}$	$m_{ll} \geqslant 20$MeV	$m_{ll} \geqslant 140$MeV
$Ds_{\mu 2ee}$	1.07×10^{-6}	2.41×10^{-8}	2.56×10^{-7}	3.95×10^{-8}
$Ds_{e2\mu\mu}$	5.46×10^{-9}	–	–	–

Table 2. In the SM framework, similar cuts in the di-lepton mass for the BR(Ds_{j2ii}), used in the decay width calculations for IB+SD contributions.

bosons, may be fully restricted by these observables if we assume the standard scenario for the computation of the χ relic density, described in section 3.8. On the other hand, the theories where the X_μ bosons are coupled to the fermion fields through both vector and axial-vector currents (Z' bosons) are not in conflict with the limits from the neutrino trident production, but can still be ruled out by $(g-2)_e$. However, a possible interference between the vector and axial-vector couplings might make the shift in the fine structure constant negligible. Under this condition a certain choice of parameters can be found for three tuned planes, which allow the explanation of the $(g-2)_\mu$ discrepancy for specific values of the c_β angle. In particular, the pairs $\kappa = -\frac{7}{5}$ for $c_\beta > 0.7$, $\kappa = 3$ for $c_\beta > 0.99$ and $\kappa = \frac{3}{2}$ for $c_\beta > 0.95$, solve the discrepancy in the muon system without the introduction of light scalars.

We propose to measure the forward-backward asymmetry in $e^+e^- \to \bar{f}f$, for $f = \mu, \tau$, far from the Z boson peak at low energies. We also suggest the measurement of the branching ratios to the purely leptonic meson decays $M \to j\nu ll$, for $M = D, D_s, B$. The ratio BR($M \to j\nu_j \mu^+\mu^-$)/BR($M \to j\nu_j e^+e^-$) in definite regions of the di-lepton invariant mass shows a deviation from the SM prediction and might serve as an important test of lepton flavour universality, in particular for $M = B$ and $j = \tau$.

Acknowledgments

We are grateful to Dmitri Melhikhov for providing us with the form-factors present in the $D_s \to \mu\nu ee$ amplitude. S.F. acknowledges support of the Slovenian Research Agency under the core funding grant P1-0035. F.C.C. would like to thank Clara H. Feliu, prof. Gudrun Hiller, Peter Schuh, Dennis Loose, Mathias Becker, Andrey Tayduganov, prof. Emmanuel A. Paschos and prof. Heinrich Päs for useful discussions. F.C.C acknowledges support from the BMBF grant "Verbundprojekt 05H2015: Quark-Flavor-Physik am LHC (BMBF-FSP 105), Flavorsignaturen in Theorie und Experiment - LHCb: Run 2 and Upgrade" and from the Technische Universität Dortmund, Department of Physics.

JHEP10(2019)279

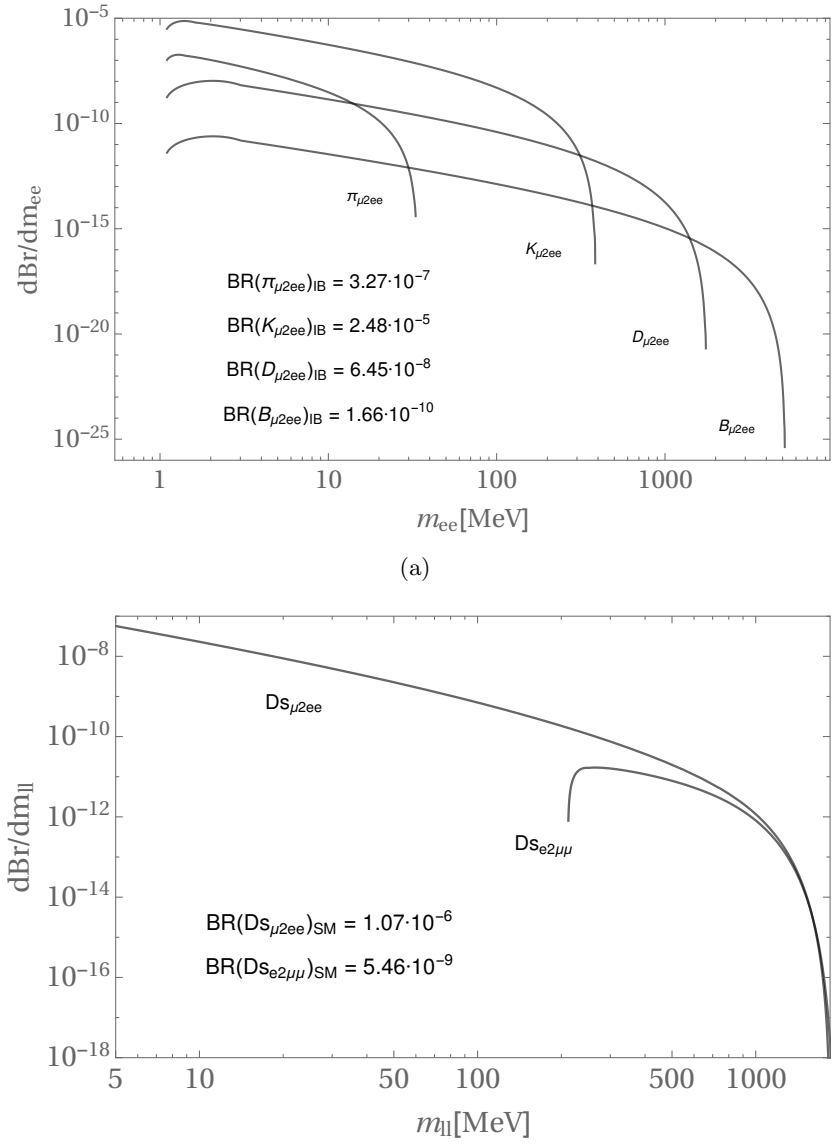

Figure 11. Differential branching ratio as a function of the di-lepton invariant mass in the SM. In the plot (a), the IB diagrams are dominant. In (b), the IB and SD contributions are presented for D_s decays.

A Feynman rules

The Feynman rules for the vertexes presented figure 1(a,b) may be generically written as

$$M^+(k)\ \bar{\nu}_l(p_i)\ l(p_j)\ :\ -i\frac{G_F}{\sqrt{2}} f_M V^*_{\rm UD}\ \not{k}(1-\gamma_5), \tag{A.1}$$

$$X_\mu(p_m)\ \bar{l}(p_i)\ l(p_j)\ :\ i\frac{\gamma_\mu}{2}(x^l_V + x^l_A\gamma_5), \tag{A.2}$$

$$X^\mu(p_m)\ M^+(p_i)\ M^-(p_j)\ :\ -ic^2_\phi\kappa\ (p^\mu_i + p^\mu_j). \tag{A.3}$$

JHEP10(2019)279

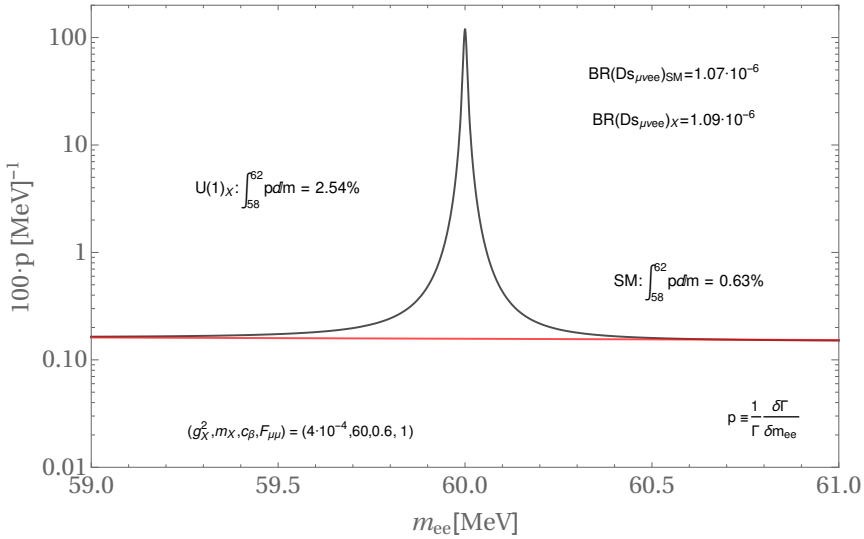

Figure 12. The normalized differential branching ratio corresponds to the probability $P = 2.54\%$ of measuring the di-lepton mass in the interval 58 MeV $< m_{ee} <$ 62 MeV at the resonance $(g_X^2, m_X) = (4 \times 10^{-4}, 60)$, one allowed region from figure 9 (a). $P = 0.63\%$, in the SM framework.

B Decay width

The general expression for the decay width can be written as

$$d\Gamma = \sum_{sp} \frac{|\mathcal{M}|^2}{2M} \frac{\Phi_n(M; m_1, \cdots, m_n)}{(2\pi)^{(3n-4)}}, \tag{B.1}$$

such that, for $n = 3$, following results of ref. [33],

$$\Phi_3(M; m_1, m_2, m_3) = dM_2^2 \Bigg|_{(m_1+m_2)^2}^{(M-m_3)^2} \frac{\sqrt{\lambda(M^2, M_2^2, m_3^2)}}{8M^2} d\Omega_3^* \frac{\sqrt{\lambda(M_2^2, m_1^2, m_2^2)}}{8M_2^2} d\Omega_2^*. \tag{B.2}$$

The variables defining the solid angle $d\Omega_i^*$ are in the rest frame of $k_i = \sum_{j=1}^{i} p_j$, $M_i^2 \equiv k_i^2$. The scalar products emerging from the squared amplitudes can be expressed in a more convenient form through the momenta k_i, i.e.

$$k_1^2 = 0, \qquad k_2^2 = M_2^2, \qquad k_3^2 = M^2 \tag{B.3}$$

and

$$k_1 \cdot k_2 = \frac{M_2^2 - m_X^2}{2}, \qquad k_2 \cdot k_3 = \frac{M^2 + M_2^2 - m_l^2}{2} \tag{B.4a}$$

$$k_1 \cdot k_3 = \frac{(k_1 \cdot k_2)(k_2 \cdot k_3)}{M_2^2} - \frac{(k_1 \cdot k_2)\sqrt{(k_2 \cdot k_3)^2 - M^2 M_2^2}}{M_2^2} c_\theta^*. \tag{B.4b}$$

Using these invariants it follows that $q^2 = m_X^2 + m_l^2 - M_2^2 + 2k_1 \cdot k_3$ and $q_{23}^2 = M^2 - 2k_1 \cdot k_3$.

JHEP10(2019)279

C Phase space integration for the neutrino trident production

The integration limits for t_i are obtained from the condition

$$\begin{aligned} t_2: &\quad G(s_2, t_2, m_3^2, t_1, m_b^2, m_2^2) \leq 0 \\ t_1: &\quad G(s, t_1, s_2, m_a^2, m_b^2, m_1^2) \leq 0 \end{aligned} \tag{C.1}$$

where G is the Cayley determinant:

$$G(x, y, z, u, v, w) = -\frac{1}{2} \begin{vmatrix} 0 & 1 & 1 & 1 & 1 \\ 1 & 0 & v & x & z \\ 1 & v & 0 & u & y \\ 1 & x & u & 0 & w \\ 1 & z & y & w & 0 \end{vmatrix}. \tag{C.2}$$

All the possible scalar products in the real photon-neutrino scattering can be written in terms of the invariants of eq. (3.59) and it is convenient to write s_1 in terms of the polar angle via

$$\begin{aligned} s_1 = s + m_3^2 - \frac{1}{\lambda(s_2, t_1, m_b^2)} \Bigg[& \begin{vmatrix} 2m_b^2 & s_2 - t_1 + m_b^2 & m_b^2 + m_3^2 - t_2 \\ s_2 - t_1 + m_b^2 & 2s_2 & s_2 - m_2^2 + m_3^2 \\ s - m_a^2 + m_b^2 & s + s_2 - m_1^2 & 0 \end{vmatrix} \\ & + 2 \left(G(s, t_1, s_2, m_a^2, m_b^2, m_1^2) G(s, t_1, s_2, m_a^2, m_b^2, m_1^2) \right)^{1/2} \cos\phi \Bigg]. \end{aligned} \tag{C.3}$$

The remaining angles in eq. (B.2) may be integrated directly and Φ_3 is reduced to

$$\Phi_3(M; m_1, m_2, m_3) = \frac{\pi^2}{4M^2} dM_2 \Bigg|_{(m_1+m_2)}^{(M-m_3)} dc_\theta^* \Bigg|_{-1}^{1} \frac{\sqrt{\lambda(M^2, M_2^2, m_3^2)} \sqrt{\lambda(M_2^2, m_1^2, m_2^2)}}{M_2}. \tag{C.4}$$

Open Access. This article is distributed under the terms of the Creative Commons Attribution License (CC-BY 4.0), which permits any use, distribution and reproduction in any medium, provided the original author(s) and source are credited.

References

[1] F.C. Correia and S. Fajfer, *Restrained dark* U(1)$_d$ *at low energies*, *Phys. Rev.* **D 94** (2016) 115023 [arXiv:1609.00860].

[2] F.S. Queiroz and W. Shepherd, *New physics contributions to the muon anomalous magnetic moment: a numerical code*, *Phys. Rev.* **D 89** (2014) 095024 [arXiv:1403.2309] [INSPIRE].

[3] W. Altmannshofer, S. Gori, M. Pospelov and I. Yavin, *Neutrino trident production: a powerful probe of new physics with neutrino beams*, *Phys. Rev. Lett.* **113** (2014) 091801 [arXiv:1406.2332] [INSPIRE].

[4] K.S. Babu, A. Friedland, P.A.N. Machado, and I. Mocioiu, *Flavor gauge models below the Fermi scale*, *JHEP* **12** (2017) 096 [arXiv:1705.01822].

JHEP10(2019)279

[5] J.L. Feng et al., *Particle physics models for the* 17 *MeV anomaly in beryllium nuclear decays*, *Phys. Rev.* **D 95** (2017) 035017 [arXiv:1608.03591].

[6] B. Batell, D. McKeen and M. Pospelov, *New parity-violating muonic forces and the proton charge radius*, *Phys. Rev. Lett.* **107** (2011) 011803 [arXiv:1103.0721] [INSPIRE].

[7] M. Pospelov, *Secluded* U(1) *below the weak scale*, *Phys. Rev.* **D 80** (2009) 095002 [arXiv:0811.1030] [INSPIRE].

[8] P.J. Fox, R. Harnik, J. Kopp and Y. Tsai, *LEP shines light on dark matter*, *Phys. Rev.* **D 84** (2011) 014028 [arXiv:1103.0240] [INSPIRE].

[9] A. Ismail, W.Y. Keung, K.H. Tsao and J. Unwin, *Axial vector Z' and anomaly cancellation*, *Nucl. Phys.* **B 918** (2017) 220 [arXiv:1609.02188].

[10] S. Baum and N.R. Shah, *Two Higgs doublets and a complex singlet: disentangling the decay topologies and associated phenomenology*, *JHEP* **12** (2018) 044 [arXiv:1808.02667].

[11] M. Dutra et al., *MeV dark matter complementarity and the dark photon portal*, *JCAP* **03** (2018) 037 [arXiv:1801.05447].

[12] Y. Kahn, G. Krnjaic, S. Mishra-Sharma and T.M.P. Tait, *Light weakly coupled axial forces: models, constraints, and projections*, *JHEP* **05** (2017) 002 [arXiv:1609.09072].

[13] J. Alexander et al., *Dark sectors 2016 workshop: community report*, arXiv:1608.08632.

[14] P. Gondolo and G. Gelmini, *Cosmic abundances of stable particles: Improved analysis*, *Nucl. Phys.* **B 360** (1991) 145 [INSPIRE].

[15] Particle Data Group collaboration, *Review of particle physics*, *Chin. Phys.* **C 40** (2016) 100001.

[16] A. Antognini et al., *Theory of the 2S-2P Lamb shift and 2S hyperfine splitting in muonic hydrogen*, *Ann. Phys.* **331** (2013) 127 [arXiv:1208.2637] [INSPIRE].

[17] N. Bezginov et al., *A measurement of the atomic hydrogen lamb shift and the proton charge radius*, *Science* **365** (2019) 1007.

[18] P.J. Mohr, B.N. Taylor and D.B. Newell, *Codata recommended values of the fundamental physical constants: 2010*, *Rev. Mod. Phys.* **84** (2012) 1527.

[19] D. Tucker-Smith and I. Yavin, *Muonic hydrogen and MeV forces*, *Phys. Rev.* **D 83** (2011) 101702 [arXiv:1011.4922] [INSPIRE].

[20] K. Pachucki, *Theory of the Lamb shift in muonic hydrogen*, *Phys. Rev.* **A 53** (1996) 2092 [INSPIRE].

[21] C.Y. Pang, R.H. Hildebrand, G.D. Cable and R. Stiening, *Search for rare k^+ decays. I. $k^+ \to \mu^+\nu\bar{\nu}\nu$*, *Phys. Rev.* **D 8** (1973) 1989 [INSPIRE].

[22] J.P. Leveille, *The second order weak correction to $(g-2)$ of the muon in arbitrary gauge models*, *Nucl. Phys.* **B 137** (1978) 63 [INSPIRE].

[23] U. Haisch, J.F. Kamenik, A. Malinauskas and M. Spira, *Collider constraints on light pseudoscalars*, *JHEP* **03** (2018) 178 [arXiv:1802.02156].

[24] W. Czyz, G.C. Sheppey and J.D. Walecka, *Neutrino production of lepton pairs through the point four-fermion interaction*, *Nuovo Cim.* **34** (1964) 404 [INSPIRE].

[25] P. Ballett et al., *Neutrino trident scattering at near detectors*, arXiv:1807.10973.

JHEP10(2019)279

[26] P. Ballett et al., *Z's in neutrino scattering at DUNE*, *Phys. Rev.* **D 100** (2019) 055012 [arXiv:1902.08579].

[27] CHARM-II collaboration, *First observation of neutrino trident production*, *Phys. Lett.* **B 245** (1990) 271 [INSPIRE].

[28] E. Byckling and K. Kajantie, *Particle kinematics*, University of Jyvaskyla, Jyvaskyla, Finland (1971).

[29] R. Belusevic and J. Smith, *W-Z interference in neutrino-nucleus scattering*, *Phys. Rev.* **D 37** (1988) 2419 [INSPIRE].

[30] J. Silk et al., *Particle dark matter: observations, Models and searches*, Cambridge University Press, Cambridge U.K. (2010).

[31] WMAP collaboration, *Five-year Wilkinson Microwave Anisotropy Probe (WMAP) observations: data processing, sky maps and basic results*, *Astrophys. J. Suppl.* **180** (2009) 225 [arXiv:0803.0732] [INSPIRE].

[32] J. Bijnens, G. Ecker and J. Gasser, *Radiative semileptonic kaon decays*, *Nucl. Phys.* **B 396** (1993) 81 [hep-ph/9209261] [INSPIRE].

[33] B.P. Kersevan and E. Richter-Was, *Improved phase space treatment of massive multi-particle final states*, *Eur. Phys. J.* **C 39** (2005) 439 [hep-ph/0405248] [INSPIRE].

JHEP10(2019)279